

Magnetic and chemical interactions  
of the nearest neighbor transition  
metal impurity pairs in  
semiconductors:  
A density-functional study

(第一原理計算による半導体中の  
最隣接遷移金属不純物対の  
磁気・化学相互作用に関する研究)

Takeshi Fujita  
Specialization in Physics  
Department of Physics, Electrical and Computer Engineering  
Yokohama National University  
A thesis submitted for the degree of  
Doctor of Engineering  
Written under the direction of  
Associate Professor Hannes Raebiger

March, 2014

## Acknowledgement

I am grateful to Associate Professor Hannes Raebiger for his guidance on this work. I am also grateful to all the past and present members of the research groups of Associate Professor Hannes Raebiger and Professor Kaoru Ohno. I am obliged to Yokohama National University (YNU), and YNU department of physics, electrical and computer engineering, and YNU Kogyokai for their financial support. I thank all my friends for hanging out with me for the past several years and cheering me up. Most importantly, I thank my parents for supporting me in practical and emotional terms.

# Abstract

Magnetic and chemical interactions of the nearest neighbor transition metal impurity pairs in semiconductors have been studied over the past few decades in order to understand, and ultimately control magnetic properties of transition metal doped semiconductors in the search for novel magnetic materials. For the mechanisms of these pairwise interactions, several pictures based on conventional phenomenological models have been presented. However, these pictures can only partially capture trends in these pairwise interactions and have not even given a congruous view of these pairwise interactions for the very same materials. This thesis tackles the issues of the mechanisms of these pairwise interactions based on density functional theory calculations.

Density functional theory calculations are among the most widely used *ab initio* electronic structure approaches today, particularly in the condensed matter physics community. By using such calculations, one can obtain electronic structure as solution to the fundamental many-electron-ion Hamiltonian instead of presupposing the preferred type of electronic interactions. Therefore, the calculations may allow us to identify the important factors for the mechanisms of these pairwise interactions that are omitted in the formulation of the conventional phenomenological models, and may unveil the true mechanisms underlying the observed different types of magnetic interactions.

We first reveal that a peculiar ferromagnetic coupling of the Cr impurity pairs in AlN that cannot be interpreted by conventional magnetic models is mainly due to *d-d* interactions that are usually assumed to be negligible. Next, we reveal for what kind of materials *d-d* interactions become important in the description of pairwise magnetic and chemical interactions of the TM impurities in III-V semiconductors.

## List of publications

This thesis consists of an overview and the following publications:

- I H. Raebiger and T. Fujita,  
"Multiple exchange interactions induced by Jahn-Teller distortions in dilute magnetic semiconductors,"  
Phys. Rev. B **84**, 172406 (2011).
  
- II H. Nakayama, T. Fujita, H. Raebiger,  
"Magnetic Properties and Stability of Quasi-One-Dimensional Cr Chains Embedded in (Zn,Cr)Te,"  
Appl. Phys. Express **6**, 073006:1-3 (2013).
  
- III H. Raebiger, H. Nakayama, and T. Fujita,  
"Control of defect binding and magnetic interaction energies in dilute magnetic semiconductors by charge state manipulation,"  
J. Appl. Phys. **115**, 012008 (2014).
  
- IV T. Fujita and H. Raebiger  
"Direct d-d interactions among transition metal impurities in III-V semiconductors,"  
(Appl. Phys. Express **7**, 023004 (2014))

In Publication I, the author has carried out all calculations, analyzed the data, and contributed significantly to writing the paper and designing the story. In Publications II and III, the author has contributed to designing the studies, supervising the calculations, and writing of the paper. In Publication IV, the author has been the corresponding author and has had central responsibility in all calculations, analyzing the data, writing the paper, designing the story. Publications I and IV are directly related to Chapters 3 and 4, respectively. Publications II and III are referred in Chapter 6 for emphasizing the importance of the findings summarized in this thesis from application point of view.



# Contents

<b>Acknowledgement</b>	<b>i</b>
<b>Abstract</b>	<b>ii</b>
<b>List of publications</b>	<b>iii</b>
<b>1 Introduction</b>	<b>1</b>
<b>2 <i>Ab initio</i> calculation of electronic structure</b>	<b>3</b>
2.1 Electronic structure calculations . . . . .	3
2.2 Density-functional theory . . . . .	4
2.3 Kohn-Sham equations . . . . .	6
2.4 Exchange-correlation functionals . . . . .	7
2.5 Projector-augmented wave (PAW) method . . . . .	7
2.6 Summary . . . . .	8
<b>3 The charge neutral Cr impurities in AlN</b>	<b>9</b>
3.1 Computational details . . . . .	9
3.2 Bulk AlN . . . . .	10
3.3 An isolated charge neutral Cr impurity in AlN . . . . .	10
3.4 The charge neutral Cr impurity pairs in AlN . . . . .	12
3.5 Summary . . . . .	16
<b>4 The charge neutral TM impurities in III-V semiconductors</b>	<b>17</b>
4.1 Computational details . . . . .	17
4.2 Bulk III-V semiconductors . . . . .	18
4.3 Isolated charge neutral TM impurities in III-V semiconductors . . . . .	18
4.4 The charge neutral TM impurity pairs in III-V semiconductors . . . . .	21
4.5 Summary . . . . .	23
<b>5 The charged TM impurities in insulators</b>	<b>25</b>
5.1 Computational details . . . . .	25
5.2 Bulk insulators . . . . .	26
5.3 Isolated charged TM impurities in insulators . . . . .	26
5.4 The charged TM impurity pairs in insulators . . . . .	27
5.5 Summary . . . . .	30

<b>6</b>	<b>Summary and outlook</b>	<b>31</b>
	<b>Appendices</b>	<b>33</b>
<b>A</b>	<b>Models for the pairwise magnetic interaction</b>	<b>34</b>
A.1	Open shell models . . . . .	34
A.2	Superexchange models . . . . .	34
<b>B</b>	<b>Way to determine parameters</b>	<b>35</b>
B.1	$U$ and $J$ parameters . . . . .	35
B.2	Cutoff energy and $\vec{k}$ -point meshes . . . . .	37
<b>C</b>	<b>Description of defect levels in the band gap of TM impurities</b>	<b>38</b>
C.1	An isolated TM impurity . . . . .	38
C.2	TM impurity pairs . . . . .	39
<b>D</b>	<b>Finite-size effects due to charged defects</b>	<b>40</b>

# 1 Introduction

Spintronics is an emerging technology that exploits both the spins of an electron and the fundamental charge of an electron. This new branch of technology may lead to completely new devices that adopt merits of both conventional electronic and magnetic devices. Conventional electronic devices, which exploit only the charge of an electron, are usually used for manipulation and transfer of information (e.g, transistors manipulate information by amplifying, rectifying and controlling the electron flow). Conventional magnetic devices rely on (ferro) magnetic metals, and exploit only the spin of an electron in the magnetized metal. The conventional magnetic devices are usually used for storage of information (e.g, magnetic tape records information by magnetizing the tape, and reads information by utilizing inductive current in a conductor induced between the conductor and magnetized tape). In magnetized conductor, electrons scatter differently depending on whether they are spin up or spin down, and the conductivity is, thus, different between spin up and spin down electrons. The current whose conductivity is different between spin up and spin down electrons is called spin-polarized current. Some spintronic devices have been used in industry exploit this spin-polarized current in the magnetized conductor to storage information (e.g, hard disk drive (HDD) ). In industry, more and more interest has been attracted to new materials for spintronic devices.

As materials with great hope for novel spintronics devices, diluted magnetic semiconductors (DMSs) have vigorously been studied over the past few decades. In these DMSs a small amount of magnetic ions ( $\sim 10^{21}\text{cm}^{-3}$ ) are introduced into non-magnetic semiconductors in order to make them magnetic. Some of DMSs show novel magnetic properties (e.g., In GaAs:Mn , the strength of ferromagnetism can be controlled by the amount of charge carriers [1]). Such novel magnetic properties are envisioned to yield new spintronic applications (e.g., when one changes carrier concentration by some external means as in conventional electronics, and one can thus change the magnetic interactions between the localized spins). One of the requirements of the practical realization of DMSs for spintronic applications is to manufacture DMSs with high Curie temperatures  $T_c$  over room temperature. Although high  $T_c$  (or blocking temperatures  $T_b$ ) over room temperature have been reported in a number of DMSs since the first reported on  $\text{TiO}_2\text{:Co}$  [2], the practical use of DMSs has still not been achieved due to low reproducibility in manufacture of DMSs with higher  $T_c$  above room temperature. For improving the reproducibility, it is required to study the magnetic properties of DMSs

in more detail.

In order to understand the origin of the magnetic properties of DMSs, density functional theory (DFT) calculations are often used. DFT calculations are among the most widely used *ab initio* electronic structure approaches today, particularly in the condensed matter physics community. By using such calculations, one can obtain electronic structure as solution to the fundamental many-electron-ion Hamiltonian instead of presupposing the preferred type of electronic interactions. Therefore, the calculations allow us to screen systematically a large range of systems and properties to identify underlying relations and hidden rules. Indeed, the calculations suggested that a key factor to affect the magnetic properties of DMSs is TM distribution (i.e., TM clustering and/or phase separation) [3], before the TM distribution has been recognized as the key factor only recently owing to the development of element-specific nano-characterization tools (e.g., synchrotron x-ray diffraction) [4].

In this thesis, we investigate the magnetic and chemical interactions of a range of the nearest neighbor substitutional TM impurity pairs in various semiconductors by using DFT calculations. Understanding these pairwise interactions is a minimum requirement to understand the relation between the magnetic properties and TM distribution. For TM impurities in semiconductors, TM impurities preferentially substitute the host cation sites as reported in both experiments (e.g., GaN:Mn [5]) and theories (e.g., GaAs:Mn [6]), and the probability of two or more TM impurities on one of the sublattices in a zinc blende, wurtzite, or rock salt crystal occupying nearby sites is  $> 50\%$  (neglecting TM-TM attractions) as for a real TM concentration [7].

The remainder of this thesis is organized as follows. Chapter 2 provides the theoretical background of the electronic structure calculations used. In Chapter 3, the study of the magnetic and chemical interactions of Cr impurity pairs in AlN for charge neutral condition is presented. In Chapter 4, the study of the magnetic and chemical interactions of TM impurity pairs in III-V semiconductors for charge neutral condition is presented. In Chapter 5, the study of the magnetic and chemical interactions of TM impurity pairs in insulators for various charged conditions is presented. Finally, a short summary of the whole thesis and the outlook for the future research direction is presented. Supplemental materials to this thesis are included in the appendices.

## 2 *Ab initio* calculation of electronic structure

In this chapter, our *ab initio* approaches for calculating electronic structure of a many-body system is introduced. In Section 2.1, the fundamental theoretical background of calculating the electronic structure is introduced. In Section 2.2, the density-functional theory (DFT) is introduced for calculating the electronic structure. In Section 2.3, a practical approach to DFT is presented. In Section 2.4, a class of approaches and necessary approximations are introduced. Section 2.5 describes the basis set for wave functions. In Section 2.6, a summary of this chapter is presented.

### 2.1 Electronic structure calculations

A major goal of electronic structure calculations is to solve the non-relativistic timeindependent Schrödinger equation;

$$\hat{H}\Psi = E\Psi , \quad (1)$$

where  $\hat{H}$  is the Hamiltonian operator,  $\Psi$  is a certain wave function, and  $E$  is the energy corresponding to  $\Psi$ , respectively. For a system consisting of  $N$  electrons and  $M$  nuclei (or ions) within the Born-Oppenheimer (BO) approximation that is usually used in quantum chemistry and related fields, the Hamiltonian operator can be written (using Hartree atomic units) as

$$\begin{aligned} \hat{H} &= \hat{T} + \hat{V}_{\text{int}} + \hat{V}_{\text{ei}} + \hat{V}_{\text{ii}} \\ &= -\frac{1}{2} \sum_{i=1}^N \nabla_i^2 + \frac{1}{2} \sum_{i \neq j}^N \frac{1}{|\mathbf{r}_i - \mathbf{r}_j|} - \sum_{i=1}^N \sum_{I=1}^M \frac{Z_I}{|\mathbf{r}_i - \mathbf{R}_I|} \\ &\quad + \frac{1}{2} \sum_{I \neq J}^M \frac{Z_I Z_J}{|\mathbf{R}_I - \mathbf{R}_J|} , \end{aligned} \quad (2)$$

where  $\hat{T}$ ,  $\hat{V}_{\text{int}}$ ,  $\hat{V}_{\text{ei}}$ , and  $\hat{V}_{\text{ii}}$  are the kinetic energy, Coulomb electron–electron potential, electron–ion potential, ion–ion potential operators respectively, with  $Z_I$  the charge of the nuclei and  $\mathbf{r}_i$  ( $\mathbf{R}_I$ ) the position vectors of the electrons (ions). Here, the final term, the repulsion between ions, can be treated as a constant for a fixed configuration of the ions. For this system within the BO approximation, the wave function can be written as

$$\Psi = \Psi(\mathbf{r}_1, \sigma_1, \dots, \mathbf{r}_N, \sigma_N) , \quad (3)$$

where the  $\mathbf{r}_i$  and  $\sigma_i$  are the position of the electron  $i$  and the  $z$ -component of spin angular momentum of the electron  $i$ , respectively. The total energy is the expectation value of the Hamiltonian,

$$\begin{aligned} E &= \frac{\langle \Psi | \hat{H} | \Psi \rangle}{\langle \Psi | \Psi \rangle} \\ &= \langle \Psi | \hat{T} | \Psi \rangle + \langle \Psi | \hat{V}_{\text{int}} | \Psi \rangle + \int V_{\text{ei}}(\mathbf{r})n(\mathbf{r})d^3\mathbf{r} + E_{ii} , \end{aligned} \quad (4)$$

where  $n(\mathbf{r})$  is the total electron density and  $E_{ii}$  is the electrostatic ion-ion interaction. The ground state energy  $E_0$  is obtained from minimizing it with respect to all the parameters in  $\Psi$ , with the constraint that  $\Psi$  must obey the particle symmetry and any conservation laws.

## 2.2 Density-functional theory

In the preceding section, we see that many body wave functions that depend on  $4N$  variables are required for calculating the total energy of the  $N$  electron system. This severely limits the system sizes in the calculation. The theory that allow us to use the total electron density that always depends on 3 variables for the calculation is the density functional theory (DFT) [8–10]. DFT is consist of the theorem by Hohenberg and Kohn (HK) and the theorems by Levy and Lieb (LL).

**Theorem by HK:** If  $n'_0(\mathbf{r}) \neq n_0(\mathbf{r})$ ,  $v'(\mathbf{r}) \neq v(\mathbf{r}) + \text{const}$ , where  $n_0(\mathbf{r})$  and  $n'_0(\mathbf{r})$  are densities associated with ground states in the external potentials  $v(\mathbf{r})$  and  $v'(\mathbf{r})$ , respectively.

**Proof :** Let  $v(\mathbf{r})$  and  $v'(\mathbf{r})$  respectively have the manifold of ground state wavefunction  $\{\Psi_0\}$  with energy  $E_0$  and the manifold of ground state wavefunction  $\{\Psi'_0\}$  with energy  $E'_0$ . Clearly, no nontrivial function in  $\{\Psi_0\}$  can belong to  $\{\Psi'_0\}$ , since  $\{\Psi_0\}$  satisfy different Schrödinger equations than  $\{\Psi'_0\}$ . Let us assume that a ground state  $\Phi$  that are linear combination of some wavefunction  $\Psi_0$  of  $\{\Psi_0\}$  and a ground state  $\Phi'$  that are linear combination of some wavefunction  $\Psi'_0$  of  $\{\Psi'_0\}$  have the same density  $n_0(\mathbf{r})$ . Let us write the two Hamiltonian operators associated, respectively, with  $v(\mathbf{r})$  and  $v'(\mathbf{r})$  as

$$\hat{H} = \hat{T} + \hat{V}_{\text{int}} + V \text{ and } \hat{H}' = \hat{T} + \hat{V}_{\text{int}} + \hat{V}' , \quad (5)$$

where  $V$  and  $V'$  are the different external potential operators. By the Rayleigh-Ritz principle we have

$$E_0 = \langle \Phi | \hat{H} | \Phi \rangle < \langle \Phi' | \hat{H} | \Phi' \rangle = E'_0 + \int (v(\mathbf{r}) - v'(\mathbf{r}))n'_0(\mathbf{r})d\mathbf{r} \quad (6)$$

and

$$E'_0 < E_0 + \int (v'(\mathbf{r}) - v(\mathbf{r}))n_0(\mathbf{r})d\mathbf{r} ; \quad (7)$$

hence,  $E_0 + E'_0 < E'_0 + E_0$  showing that the initial assumption was false. Note that the variational estimates are strictly larger than the corresponding eigenvalues, because,  $\{\Psi_0\} \cap \{\Psi'_0\}$  is empty.

**Theorem 1 by LL:**  $\int v(\mathbf{r})n(\mathbf{r})d\mathbf{r} + Q[n] \geq E_0$ , where  $Q[n] = \langle \Psi_{\min}^n | \hat{T} + \hat{V}_{\text{int}} | \Psi_{\min}^n \rangle$  and  $\Psi_{\min}^n$  is the wavefunction that minimizes  $\langle \Psi^n | \hat{T} + \hat{V}_{\text{int}} | \Psi^n \rangle$  for a fixed  $n$ .

**Proof:** The minimum total energy for an arbitrary density  $n$  is given by

$$\int v(\mathbf{r})n(\mathbf{r})d\mathbf{r} + Q[n] = \langle \Psi_{\min}^n | \hat{T} + \hat{V}_{\text{int}} + \hat{V} | \Psi_{\min}^n \rangle . \quad (8)$$

By the Rayleigh-Ritz principle we have

$$\langle \Psi_{\min}^n | \hat{T} + \hat{V}_{\text{int}} + \hat{V} | \Psi_{\min}^n \rangle \geq E_0 . \quad (9)$$

Finally, combining eq. 8 and eq. 9 completes the proof.

**Theorem 2 by LL:**  $\int v(\mathbf{r})n_0(\mathbf{r})d\mathbf{r} + Q[n_0] = E_0$ , where  $Q[n_0] = \langle \Psi_{\min}^{n_0} | \hat{T} + \hat{V}_{\text{int}} | \Psi_{\min}^{n_0} \rangle$  and  $\Psi_{\min}^{n_0}$  is the wavefunction that minimizes  $\langle \Psi^{n_0} | \hat{T} + \hat{V}_{\text{int}} | \Psi^{n_0} \rangle$  for the ground state density  $n_0$ .

**Proof:** By the Rayleigh-Ritz principle,

$$\langle \Psi_0 | \hat{T} + \hat{V}_{\text{int}} + \hat{V} | \Psi_0 \rangle \leq \langle \Psi_{\min}^{n_0} | \hat{T} + \hat{V}_{\text{int}} + \hat{V} | \Psi_{\min}^{n_0} \rangle , \quad (10)$$

or

$$\int v(\mathbf{r})n_0d\mathbf{r} + \langle \Psi_0 | \hat{T} + \hat{V}_{\text{int}} | \Psi_0 \rangle \leq \int v(\mathbf{r})n_{\text{gs}}(\mathbf{r})d\mathbf{r} + \langle \Psi_{\min}^{n_0} | \hat{T} + \hat{V}_{\text{int}} | \Psi_{\min}^{n_0} \rangle , \quad (11)$$

which leads to

$$\langle \Psi_0 | \hat{T} + \hat{V}_{\text{int}} | \Psi_0 \rangle \leq \langle \Psi_{\min}^{n_0} | \hat{T} + \hat{V}_{\text{int}} | \Psi_{\min}^{n_0} \rangle . \quad (12)$$

But, the definition of  $\Psi_{\min}^{n_0}$  dictates that

$$\langle \Psi_0 | \hat{T} + \hat{V}_{\text{int}} | \Psi_0 \rangle \geq \langle \Psi_{\min}^{n_0} | \hat{T} + \hat{V}_{\text{int}} | \Psi_{\min}^{n_0} \rangle . \quad (13)$$

The last two equations hold simultaneously if and only if

$$\langle \Psi_0 | \hat{T} + \hat{V}_{\text{int}} | \Psi_0 \rangle = Q[n_0] . \quad (14)$$

Now,

$$E_0 = \int v(\mathbf{r})n_0d\mathbf{r} + \langle \Psi_0 | \hat{T} + \hat{V}_{\text{int}} | \Psi_0 \rangle . \quad (15)$$

Finally, substitution of eq. 14 into eq. 15 completes the proof.

In summary, DFT allows us to state the following.

- a The energies  $E$  in eq. 4 can be explicitly written as a function of the electron density  $n(\mathbf{r})$ , i.e.,  $E[n]$ .
- b The ground state energy  $E_0$  and density  $n_0(\mathbf{r})$  correspond to the minimum of the functional  $E[n]$ .

### 2.3 Kohn-Sham equations

The density functional theory shows it is possible to use the ground state electron density to calculate the ground state energy, but it does not provide a way of finding the ground state density. A practical approach to this is provided by Kohn and Sham [11].

For introducing a fictitious non-interacting system that generates the same density as the interacting system, the energy functional  $E[n]$  introduced in the preceding section can be rewritten as

$$E[n] = T_s[n] + E_H[n] + E_{xc}[n] + \int V_{ei}(\mathbf{r})n(\mathbf{r})d^3\mathbf{r} + E_{ii}[n] . \quad (16)$$

Here,  $n(\mathbf{r}) = \sum_i^N |\psi_i(\mathbf{r})|^2$ ,  $T_s[n] = \sum_i^N \int \psi_i^*(\mathbf{r})(-\frac{1}{2}\nabla^2)\psi_i(\mathbf{r})d^3\mathbf{r}$ ,  $E_H[n] = \frac{1}{2} \int \int \frac{n(\mathbf{r})n(\mathbf{r}')}{|\mathbf{r}-\mathbf{r}'|} d^3\mathbf{r}d^3\mathbf{r}'$ ,  $E_{xc}[n] = \langle \Psi | \hat{T} | \Psi \rangle - T_s[n] + \langle \Psi | \hat{V}_{int} | \Psi \rangle - E_H[n]$ .

Writing the functional in eq. 16 explicitly in terms of the density built from noninteracting orbitals  $\psi(\mathbf{r})$  and applying the variational theorem as introduced in the preceding section, we find that the orbitals, which minimise the energy, satisfy the following set of equations (the Kohn-Sham equations);

$$\left(-\frac{1}{2}\nabla_i^2 + v_{eff}(\mathbf{r})\right)\psi_i(\mathbf{r}) = \varepsilon_i\psi_i(\mathbf{r}) , \quad (17)$$

where the effective potential  $v_{eff}(\mathbf{r})$  is  $V_{ei}(\mathbf{r}) + \frac{\delta E_{xc}[n]}{\delta n(\mathbf{r})} + \int \frac{n(\mathbf{r}')}{|\mathbf{r}-\mathbf{r}'|} d^3\mathbf{r}'$ . Since  $v_{eff}(\mathbf{r})$  depends on the density  $n(\mathbf{r})$  which is then computed from the (Kohn-Sham) orbitals  $\psi(\mathbf{r})$ , this equation should be solved self-consistently. Finally, the total energy can be determined from the resulting density via eq. 16.



## 2.4 Exchange-correlation functionals

The formulation of the Kohn-Sham (KS) equations is in principle exact, but the exchange-correlation functional  $E_{\text{xc}}$  is unknown. There are many approaches to the functional  $E_{\text{xc}}$  with varying levels of complexity. We now introduce some of the common types of the approaches.

The local density approximation (LDA) is the simplest approximation to the functional;

$$E_{\text{xc}}^{\text{LDA}}[n] = \int n(\mathbf{r})f(\rho)d^3\mathbf{r} , \quad (18)$$

where  $\rho$  and  $f(\rho)$  are the local values of electron density  $n(\mathbf{r})$  and a function of the local densities, respectively.

A more sophisticated approximation is the generalized gradient approximation (GGA) in which also gradients of the local densities are taken into account;

$$E_{\text{xc}}^{\text{GGA}}[n] = \int f(\rho, \nabla\rho)d^3\mathbf{r} , \quad (19)$$

where  $f(\rho, \nabla\rho)$  is a function of the local densities and their gradients. In this study, the GGA functional by Perdew *et al.* (GGA-PBE [12]) is used.

The  $+U$  correction is a correction to the LDA/GGA functional for obtaining an accurate description of localized electronic states via using parameters;

$$E_{\text{xc}}^{\text{LDA/GGA}+U}[n, g_s] = E_{\text{xc}}^{\text{LDA/GGA}}[n] + f^U(g_s) - f^{\text{dc}}(g_s) . \quad (20)$$

Here,  $g_s$ ,  $f^U(g_s)$ , and  $f^{\text{dc}}(g_s)$  are the occupation numbers of a particular shell of orbitals, and a function of the occupation numbers that depends on the Coulomb  $U$  and exchange  $J$  parameters, a function of the occupation numbers for removing the energy contribution of the orbitals included in the LDA/GGA functional in order not to count twice their contributions, respectively. In this study, the LDA/GGA+ $U$  functional by Dudarev *et al* [13] is used.

## 2.5 Projector-augmented wave (PAW) method

For practically solving the KS equations, basis functions are required to represent the KS orbital  $\psi(\mathbf{r})$  that oscillates rapidly around atomic nuclei and runs smoothly in the interstitial region (away from the nuclei). There are many approaches to the basis functions with varying levels

of complexity. We now introduce an accurate and numerically efficient approach.

The projector augmented wave (PAW) method [14] is a calculation method which utilizes linear transformation from the pseudo (PS) wave function  $\tilde{\psi}$  that is numerically conveniently representable in a plane-wave basis to a full one-electron KS wave function  $\psi$ ;

$$|\psi\rangle = \tau|\tilde{\psi}\rangle . \quad (21)$$

On the basis of the assumption that  $\psi$  can be represented by  $\tilde{\psi}$  in the interstitial region, the transformation should be of the form,

$$\tau = 1 + \sum_a \tau^a , \quad (22)$$

where  $a$  and  $\tau^a$  are an atom index and a local operator that acts only within sphere around the atom  $a$ , respectively. Here, the spheres do not overlap each other.

Inside the spheres,  $\psi$  can be expanded in partial waves  $\phi_i^a$  and for each of the partial waves a corresponding atom-centered pseudo functions  $\tilde{\phi}_i^a$  that are numerically conveniently representable in a plane-wave basis is defined such that,

$$|\phi_i^a\rangle = (1 + \tau^a)|\tilde{\phi}_i^a\rangle \iff \tau^a|\tilde{\phi}_i^a\rangle = |\phi_i^a\rangle - |\tilde{\phi}_i^a\rangle , \quad (23)$$

for all  $i, a$ . This completely defines  $\tau^a$ , given  $\phi$  and  $\tilde{\phi}$ .

For introducing the projector functions  $p_i^a$  that act within spheres around the atoms and obey the bi-orthogonality condition  $\langle p_i^a | \tilde{\phi}_i^a \rangle = \delta_{i,j}$ , the local operator  $\tau^a$  can be rewritten as,

$$\tau^a = \sum_i (|\phi_i^a\rangle - |\tilde{\phi}_i^a\rangle) \langle p_i^a | . \quad (24)$$

The final expression for the PAW wave functions is obtained by inserting eq. 22 and eq. 24 into eq. 21;

$$|\psi\rangle = |\tilde{\psi}\rangle + \sum_a \sum_i (|\phi_i^a\rangle - |\tilde{\phi}_i^a\rangle) \langle p_i^a | \tilde{\psi}\rangle . \quad (25)$$

## 2.6 Summary

In this chapter, the concept of the density functional theory that is a useful theory for calculating electronic structure of a many-body system and practical approaches to the theory are introduced. The calculations in the Chapters 3, 4, and 5 are based on the concept and approaches introduced in this chapter.

### 3 The charge neutral Cr impurities in AlN

Cr-doped AlN, AlN:Cr henceforth, is one of transition metal (TM)-doped III-V semiconductors and reported to be ferromagnetic with sensationally high Curie temperatures [15–22] or not ferromagnetic at all [23, 24]. The "ferromagnetism" has been attributed to either phase separation [15–17]) or the lack of thereof [18–22]. To describe the magnetic properties of AlN:Cr, models for pairwise magnetic interactions that are constructed or formulated with the electronic states of the isolated TM atom based on point symmetries may be useful. For applying such models to describe the magnetic properties of TM-doped semiconductors that have deep defect levels such as AlN:Cr [5], open shell "p-d exchange" or "double exchange" models [25–28], or closed shell "superexchange" models [29–31] are usually quoted (e.g., double exchange model is quoted for description of the magnetism of AlN:Cr [20]). However, the pairwise magnetic interaction of TM-doped III-V semiconductors are reported to deviate strongly in the behavior expected from double exchange model or superexchange model [3]. This calls for a more appropriate model to describe the pairwise magnetic interaction of TM-doped III-V semiconductors. We report a case study of the pairwise magnetic and chemical interactions of Cr impurities in AlN for a charge neutral condition by using *ab initio* methods.

This chapter is structured as follows. The computation details are introduced in Section 3.1. Structural parameters of bulk AlN are discussed in Section 3.2. The atomic and electronic structures of an isolated charge neutral Cr impurity in AlN are discussed in Section 3.3. The magnetic and chemical interactions of the charge neutral Cr impurity pairs in AlN are discussed in Section 3.4. Finally, we sum up all results, draw a conclusion, and present the outlook for future studies in Section 3.5.

#### 3.1 Computational details

We consider AlN with an isolated Cr impurity and the respective nearest neighbor pair. We carry out total energy calculations within generalized gradient approximation (GGA-PBE) [12] with and without the on-site potential  $+U$  [13] to the density-functional theory together with projector augmented wave methods [14], as implemented in the VASP package [32, 33]. In the latter  $+U$  calculations, we use moderate values of  $U = 3$  eV and  $J = 1$  eV that are determined in such a way that it correctly reproduces relative stability of competing binaries as described in Appendix B.1. The defect-containing systems are modeled with wurtzite-

structured supercells of 64-96 atoms, with one or two cations replaced by a TM atom, representing the isolated impurity and nearest-neighbor pair, respectively. The plane-wave cutoff is set at 460 eV,  $k$ -point meshes of  $3\times 2\times 2$  for the 64 atom supercells and  $2\times 2\times 2$  for the 96 atom supercells. The values of these parameters are determined on the basis of the convergence criteria as described in Appendix B.2.

### 3.2 Bulk AlN

AlN is a wurtzite structure semiconductor. The basal lattice parameter is  $a$  and the axial lattice parameter is  $c$ . The internal parameter  $u$  defined as the anion-cation bond length along the (0001) axis in units of  $c$ . The equilibrium lattice constant of bulk AlN were computed and compared to experiment and previous theory as given in Table 5. The agreement with experimental and theoretical data is very good, with deviations from both experiment and theory below 1%.

Table 1: Lattice constant  $a$ , axial ratio  $c/a$ , and internal parameter  $u$  of AlN

	$a$ (Å)	$c/a$	$u$
GGA-PBE (present)	3.13	1.60	0.382
Experiment [34]	3.110	1.601	0.3821
LDA [35]	3.144	1.605	0.381
GGA-PW91 [36]	3.1095	1.6060	0.3819

### 3.3 An isolated charge neutral Cr impurity in AlN

An isolated Cr impurity in AlN induces deep defect levels in the forbidden band gap of the host that may trap carriers (electrons or holes) as shown by the calculated density of states given in Fig. 1. From Fig. 1, we see that the defect levels are non-degenerate levels and there are not any partial occupied states in the levels within both the GGA and GGA+ $U$  functionals. Moreover, we see that the 1st, 2nd, 3rd, 4th, and 5th defect levels in order of increasing energy respectively have  $d_{zx}$ ,  $d_{zy}$ ,  $d_{xy}$ ,  $d_{x^2-y^2}$ , and  $d_{z^2}$  characters within both the two functionals. The 1st and 2nd levels can be described as nonbonding levels and the 3rd, 4th, and 5th levels can be described as antibonding levels according to the description of an isolated TM-derived defect levels in the gap as introduced in Appendix C.1.

To describe the Cr-induced defect states on the basis of point symmet-

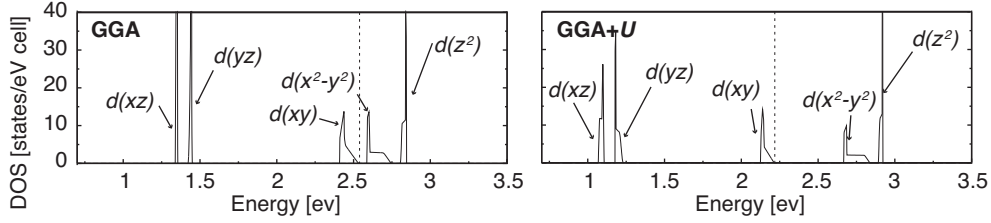
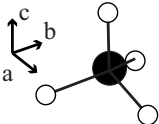


Figure 1: Total density of states (DOS) of an isolated Cr impurity in AlN for majority spin states within the GGA and GGA+ $U$  functionals. The states labeled by each  $d$ -orbitals indicate the states with strong each  $d$ -orbital characters estimated from partial charge density analysis. The energies in (a) and (b) are with respect to the valence band edge (set as zero), and the vertical dashed line denotes the highest occupied level.

ries, we first investigate the Cr-N nearest neighbor bonds to estimate the point symmetry of the Cr surrounding environment as given in Table 2. If the point symmetry of the Cr-induced defect states is consistent with the estimated point symmetry of the Cr surrounding environment, the point symmetry of the Cr-induced defect states would be  $C_{2v}$  and  $C_s$  symmetries within the GGA and GGA+ $U$  functionals, respectively. Note however that, a  $C_{2v}$  symmetry does not permit that the 3rd defect levels that can be described as the antibonding level shows  $d_{xy}$  character, because  $d_{xy}$  character must be shown in nonbonding level (due to  $\gamma$ - $p(\sigma)=2 A_1 \oplus B_1 \oplus B_2$  and  $\gamma$ - $d(\sigma)=2 A_1 \oplus A_2: d_{xy} \oplus B_1 \oplus B_2$ ). This indicates that the estimation of point groups of the Cr surrounding environment from the Cr-N nearest neighbor bond lengths lacks accuracy somewhat. We next investigate symmetry operators in total charge density of the Cr impurity. In the density, we only identify a mirror plane within both the GGA and GGA+ $U$  functionals as shown in Fig. 2. We conclude th-

Table 2: The Cr-N nearest neighbor bond lengths and the point group of the Cr surrounding environment estimated from the lengths. Cr and N atoms are shown as black white balls, respectively.

	$d(\text{Cr-N})_{ab} [\text{\AA}]$			$d(\text{Cr-N})_c [\text{\AA}]$	Sym
	GGA	1.96	1.96	1.97	1.97
GGA+ $U$	1.97	1.99	1.99	2.00	$C_s$

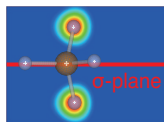


Figure 2: Iso-surface level of the total charge density with  $\sigma$ -plane.

at the point symmetry of the Cr-induced defect states is  $C_s$  symmetry within both the two functionals and describe the defect levels within both the two functionals on the basis of the symmetry as schematically illustrated in Fig. 3.

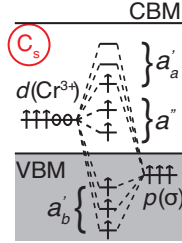


Figure 3: Schematic energy level diagram of an isolated Cr impurity in AlN for majority spin states. The horizontal line of CBM and VBM indicates conduction band minimum and valence band maximum, respectively.

### 3.4 The charge neutral Cr impurity pairs in AlN

For the nearest neighbor Cr impurity pairs in AlN, there are the two crystallographically inequivalent pairs labeled "in-plane" and "out-of-plane" depending on whether or not the Cr atoms lie within the a-b plane of the wurtzite structure as illustrated in Fig. 4.

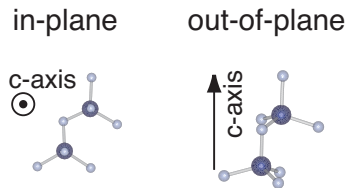


Figure 4: The "in-plane" and "out-of-plane" atomic configurations. The blue and white ball spheres denote Cr and N, respectively.

The Cr impurity pairs induce a manifold of defect levels in the gap as shown by the calculated density of states given in Fig. 5. A wide energetic range of these levels within both the GGA and GGA+ $U$  functionals corresponds to the ferromagnetic spin configurations in the ground states as previously reported in Refs. [37, 38].

From partial charge density analysis of the defect levels, we can describe the defect levels for the "in-plane" configuration due to the interaction of two isolated Cr-induced levels as schematically illustrated in Fig. 6. In the interaction for the in-plane dimer, one can see a clear sign-

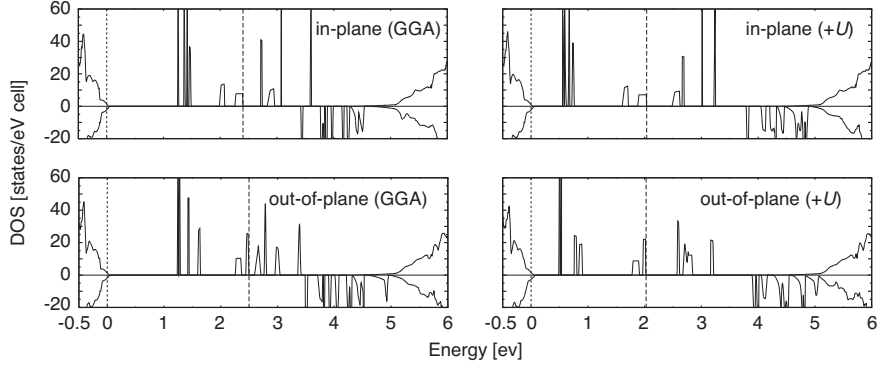


Figure 5: Total density of states (DOS) for the "in-plane" and "out-of-plane" configurations within the GGA and GGA+ $U$  functionals. The positive and negative DOS values indicate majority and minority spin DOS, respectively. The dotted line indicates the position of the host valence band maximum, and the dash line gives the position of the highest occupied state.

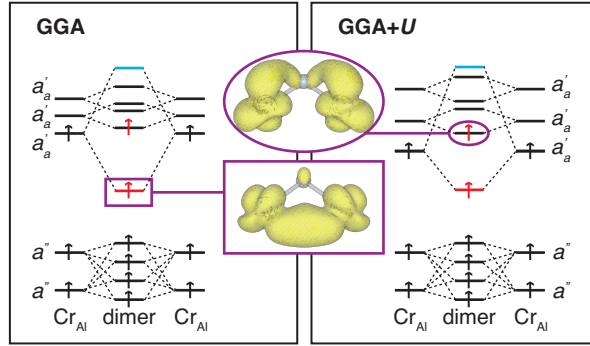


Figure 6: Schematic energy level diagram for the "in-plane" configuration within the GGA and GGA+ $U$  functionals. The middle insets show the spatial shape of the Cr-N-Cr three center and Cr-Cr two-center chemical bonds.

ature of  $d$ - $d$  interactions due to the  $d_{xy}$  derived orbitals as shown in the lower inset of Fig 6. The amount of wave function overlap can be roughly quantified by the absolute value of the "gap level charge density"  $\rho_{\text{gap}} = \sum_{\text{gap}} \psi_i^2$  due to the occupied gap levels (i.e., levels above the host valence band maximum) at the bond centers; we obtain  $0.02 \text{ e}/\text{\AA}^3$  for the in-plane dimer, and roughly half the value for the out-of-plane dimer. This difference in the absolute value of the gap charge density  $\rho_{\text{gap}}$  for the two dimers manifests a different type of bonding. Indeed, for the "out-of-plane" dimer, the  $d_{xy}$  derived orbitals are confined in different wurtzite

a-b planes with no overlap, and instead, there is a weak overlap of the  $d_{zy}$  and  $d_{z^2}$  derived orbitals, which yields a weaker bonding. Both the in-plane and out-of-plane interactions are slightly reduced by the on-site  $+U$  potential due to an increased localization, but this effect is substantially smaller than the directional variation of the interaction described above.

To investigate how such pair interactions contributes to the pairwise magnetic and chemical interactions, we calculate the pairwise magnetic coupling energy  $\Delta E$  and binding energy  $E_b$  defined as

$$\Delta E = E_{\text{F}}[\text{Cr}^{\text{a}} - \text{Cr}^{\text{b}}] - E_{\text{AF}}[\text{Cr}^{\text{a}} - \text{Cr}^{\text{b}}], \quad (26)$$

$$E_b = E_{\sigma}[\text{Cr}^{\text{a}} - \text{Cr}^{\text{b}}] - 2E[\text{Cr}] + E[\text{host}], \quad (27)$$

where  $E_{\text{Cr}^{\text{a}}-\text{Cr}^{\text{b}}}$ ,  $E_{\text{Cr}}$ , and  $E_{\text{host}}$  are respectively the total energies of the Cr pairs, the isolated Cr impurity, and the pure host, and  $\sigma$  denotes the spin alignment (F for parallel and AF for antiparallel) of the Cr pairs. The calculated energies  $\Delta E$  and  $E_b$  are given in Table 3. All the Cr-Cr pairs exhibit ferromagnetic and attractive chemical interactions. These interactions are stronger for the "in-plane" configuration than for the "out-of-plane" configuration and also stronger within the GGA functional than within the GGA+ $U$  functional. The origin of these interactions can be described due to the pair interactions as schematically illustrated in Fig. 6. In the pair interactions, each  $d_{xy}$  derived a' orbitals form a bonding and antibonding level, of which the antibonding level lies at higher energies than the previously unoccupied  $d_{x^2-y^2}$  and  $d_{z^2}$  derived a' orbitals, so the  $d_{x^2-y^2}$  one will be occupied instead. Thus, only the bonding  $d_{xy}$  derived orbital is occupied, amounting for the brunt of the energy gain shown in Table 3. The difference in the strength of the ferromagnetic interaction can be described due to the difference of the strength of  $d$ - $d$  interactions as discussed above.

Table 3: The pairwise magnetic coupling energy  $\Delta E$  and binding energy  $E_b$  for the "in-plane" and "out-of-plane" configurations within the GGA and GGA+ $U$  functionals.

$\Delta E$ [meV]	in	out	$E_b$ [meV]	in	out
GGA	-496	-239	GGA	813	507
+ $U$	-399	-168	+ $U$	510	266

We discuss the ferromagnetic interaction comparing various conventional models for ferromagnetic interactions. Within both the GGA and



GGA+ $U$  functionals, all the Cr-Cr pairs exhibit a strong ferromagnetic interaction for both the "in-plane" and "out-of-plane" configurations, albeit any partially occupied states do not exist in the isolated Cr impurity in AlN as discussed in Section 3.3. This ferromagnetic interaction without partially occupied states cannot be described with "open shell" model, which usually used to predict the magnetic interaction of the  $3d$ - $3d$  impurity dimers, where open shell configuration, i.e, partial occupancies, works as driving force for ferromagnetic interaction, as introduced in Appendix A.1.

Another popular theory of magnetic interactions is that of "superexchange". While it is usually invoked to describe antiferromagnetic interactions, it can yield ferromagnetic interactions without partial occupancies under special circumstances (e. g, the angle between  $\text{TM}^a$ -ligand- $\text{TM}^b$  is near  $90^\circ$  or one of  $\text{TM}^a$ -ligand and  $\text{TM}^b$ -ligand bonds is more ionic than the other) as introduced in Appendix A.2. Thus, the present ferromagnetic interaction without partial occupancies in Cr:AlN might be yielded by this ferromagnetic "superexchange" interaction. The necessary imbalance in the bondings can be quantified in terms of a "gap level charge"  $Q_{\text{gap}}(q)$  [39] defined as

$$Q_{\text{gap}}(q) = \int_0^R dr \rho(r) = \sum_i^{\text{gap}} \int_0^R dr \psi_i^2, \quad (28)$$

where the sum is taken only over the occupied levels  $\psi_i$  that reside within the host band gap.  $R$  is arbitrarily chosen as  $1.323 \text{ \AA}$ . These gap level charges measure the "oxidation state" of each Cr atom, which in turn quantifies the nature of the Cr-N bonding. Therefore, if  $Q_{\text{gap}}(\text{Cr}^a) = Q_{\text{gap}}(\text{Cr}^b)$ , there is no bonding imbalance, and the larger their difference  $\Delta Q_{\text{gap}} = |Q_{\text{gap}}^{\text{Cr}^a} - Q_{\text{gap}}^{\text{Cr}^b}|$  is, the more reason one has to expect for a ferromagnetic "superexchange". Likewise, the nature of the bonding is manifested in the bond lengths  $a(\text{Cr}^a - \text{N})$  and  $a(\text{Cr}^b - \text{N})$ , and to quantify their imbalance, we define  $\Delta a = |a(\text{Cr}^a - \text{N}) - a(\text{Cr}^b - \text{N})|$ . The angle between  $\text{Cr}^a$ -anion- $\text{Cr}^b$   $\angle$ ,  $\Delta a$ , and  $\Delta Q_{\text{gap}}$  are given in Table 4. The angle between  $\text{Cr}^a$ -anion- $\text{Cr}^b$  is roughly larger for parallel spin configuration than for anti-parallel spin configuration, even though the ground states are parallel spin configuration. Both  $\Delta a$  and  $\Delta Q_{\text{gap}}$  are roughly larger for the "out-of-plane" configuration than for the "in-plane" configuration, even though the pairwise magnetic coupling energy  $\Delta E$  is largest for the in-plane configuration. These are in stark contrast with any prediction from any superexchange theory, since the more orthogonally arranged and non-equivalently bon-

Table 4: The angle  $\angle$ ,  $\Delta a$ , and  $\Delta Q_{\text{gap}}$  for the "in-plane" and "out-of-plane" configurations for the parallel and anti-parallel spin configurations within the GGA and GGA+ $U$  functionals. F and AF indicates parallel and anti-parallel spin configurations, respectively.

F	in(GGA)	out(GGA)	in(+ $U$ )	out(+ $U$ )
$\angle$ [ $^\circ$ ]	106	106	105	104
$\Delta Q_{\text{gap}}$ [e]	0.00	0.08	0.00	0.32
$\Delta a$ [ $\text{\AA}$ ]	0.00	0.07	0.00	0.07

AF	in(GGA)	out(GGA)	in(+ $U$ )	out(+ $U$ )
$\angle$ [ $^\circ$ ]	103	105	106	102
$\Delta Q_{\text{gap}}$ [e]	0.43	0.72	0.17	0.04
$\Delta a$ [ $\text{\AA}$ ]	0.07	0.17	0.00	0.04

ded pairs are less ferromagnetic than the more non-orthogonally arranged and equivalently bonded pairs, this conclusion holds with either the GGA or GGA+ $U$  functionals.

### 3.5 Summary

In this chapter, the pairwise magnetic and chemical interactions of Cr impurities in AlN for a charge neutral condition are theoretically studied. The main results are summarized below;

- This pairwise magnetic interaction cannot be described with conventional models for the pairwise magnetic interaction of transition metal doped semiconductors or insulators.
- These pairwise interactions can be described mainly due to  $d$ - $d$  interactions.

These results leave open the question of whether or not there are other cases where  $d$ - $d$  interactions play an important role in the description. To this end, we investigate the pairwise magnetic and chemical interactions of a range of transition metal impurities in III-V semiconductors for a charge neutral condition as introduced in the next chapter.

## 4 The charge neutral TM impurities in III-V semiconductors

Transition metal (TM) doped III-V semiconductors have exotic magnetic properties that are intimately connected with the TM-cluster formation [4,40], and may be described starting from the pairwise magnetic and chemical interactions among the TM atoms. Usually these interactions are described via the  $p$ - $d$  hybridization of a single isolated TM impurity and the host semiconductor [4,27,28,41–49], assuming that direct  $d$ - $d$  interactions of the nearby TM atoms can be neglected [50,51]. As described in the previous chapter, this assumption has been shown to break down in some special cases, as the  $d$ - $d$  interactions become dominant [52–55]. This calls for careful reassessment of the above assumption: are there other cases where  $d$ - $d$  interactions become dominant, and if so, for what range of materials can one safely neglect the direct  $d$ - $d$  interactions? We report a systematic theoretical study of the pairwise magnetic and chemical interactions of a range of TM impurities in various III-V semiconductors for a charge neutral condition by using *ab initio* methods.

This chapter is structured as follows. The computation details are introduced in Section 4.1. Structural parameters of bulk III-V semiconductors are discussed in Section 4.2. The electronic structure of isolated charge neutral TM impurities in III-V semiconductors is discussed in Section 4.3. The magnetic and chemical interactions of the charge neutral TM impurity pairs in III-V semiconductors are discussed in Section 4.4. Finally, we sum up all results, draw a conclusion, and present the outlook for future studies in Section 4.5.

### 4.1 Computational details

We consider the series of host materials of AlX and GaX, where X = N, P, As, with an isolated TM impurity and the respective nearest neighbor pair. As TMs, we consider Ti, V, Cr, Mn, and Fe. We carry out total energy calculations within the generalized gradient approximation (GGA-PBE) [12] to the density-functional theory together with projector augmented wave methods [14], as implemented in the VASP package [32,33]. The hosts are modeled with zincblende-structured supercells of 64 atoms, with one or two cations replaced by a TM atom, representing the isolated impurity and nearest-neighbor pair, respectively. The plane-wave cutoff is set at 460 eV, 460 eV, 320 eV, 290 eV, 300 eV, and 290 eV for AlN(:TM), GaN(:TM), AlP(:TM), GaP(:TM), AlAs(:TM),

and GaAs(:TM), respectively.  $k$ -point meshes is set at  $3\times 3\times 3$ ,  $3\times 3\times 3$ ,  $2\times 2\times 2$ ,  $2\times 2\times 2$ ,  $2\times 2\times 2$ , and  $3\times 3\times 3$  for AlN(:TM), GaN(:TM), AlP(:TM), GaP(:TM), AlAs(:TM), and GaAs(:TM), respectively. These parameters are determined as described in Appendix B.2.

## 4.2 Bulk III-V semiconductors

AlN and GaN are stable in wurtzite phase and metastable in zincblende phase. The other host materials are stable in zincblende phase. For the sake of generality, we model all materials in zincblende structures. For zincblende-structured semiconductors, the basal lattice parameter is  $a$ . The equilibrium lattice constant of bulk III-V semiconductors were computed and compared to experiment and previous theory as given in Table 5. The agreement with experimental and theoretical data is very good, with deviations from experiment below 2% and theory below 1%.

Table 5: Lattice constant  $a$  of III-V semiconductors

$a$ [Å]	AlN	AlP	AlAs	GaN	Gap	GaAs
PBE (present)	4.40	5.51	5.73	4.59	5.53	5.76
PBE (Refs [56])	4.402	5.506	5.735	4.546	5.506	5.752
Experiment [57]	4.36	5.4635	5.660	4.50	5.451	5.653

## 4.3 Isolated charge neutral TM impurities in III-V semiconductors

An isolated TM impurity in a semiconductor host induces defect levels in the forbidden band gap of the host that may introduce or trap carriers (electrons or holes) as shown by the calculated density of states given in Fig. 7. The defect levels can be classified into  $e$  and/or  $t$  represented levels from the projection of the TM local density of states onto the  $e$  and  $t_2$  representations. The energies of these  $e$  and  $t$  represented levels is high for systems with a small TM atomic number  $Z$  (e.g., Ti). These  $e$  and  $t$  represented levels are occupied by the electrons due to the TM impurity, which yield the  $e^1$ ,  $e^2$ ,  $e^2t^1$ ,  $e^2t^2$ , and  $e^2t^3$  configurations respectively for Ti, V, Cr, Mn, and Fe. Note however that, the  $e^1$  states of the nitrides with Ti falsely hybridize with the conduction band due to the LDA (GGA) errors [27, 58], and thus, are not considered henceforth.

The TM induced defect levels can be described as nonbonding  $e$  levels and/or antibonding  $t$  levels in the gap due to  $p$ - $d$  (anion-TM) interactions as introduced in Appendix C.1. The nonbonding and antibonding state-

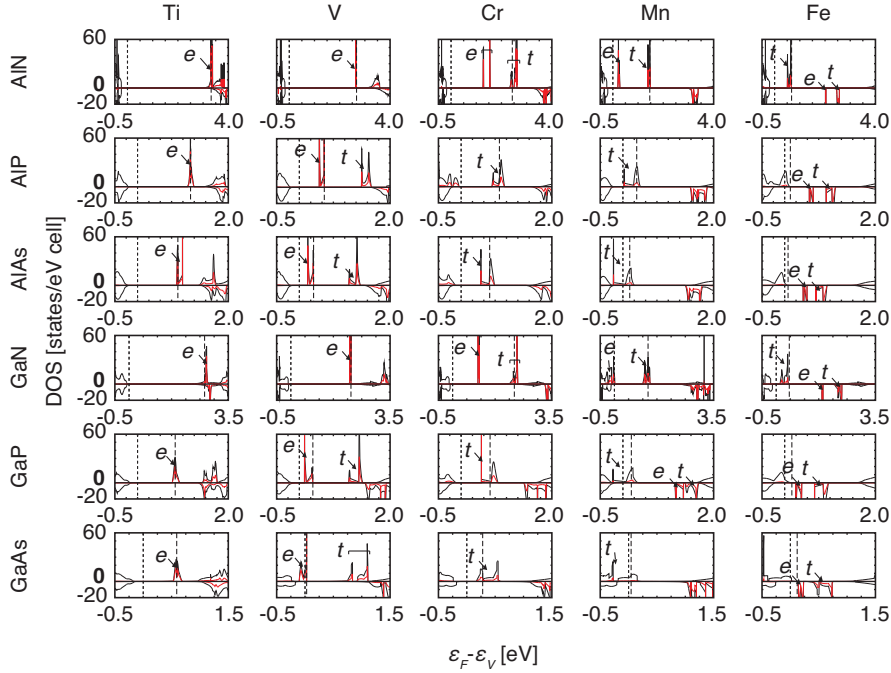


Figure 7: Spin polarized densities of states (DOS) of isolated TM impurities. The black and red lines indicate the total DOS and the transition-metal local DOS, respectively. The states labeled by  $e$  ( $t_2$ ) indicate the states with the  $e$  ( $t_2$ ) symmetry representation within the gap. The positive and negative DOS values indicate majority and minority spin DOS, respectively. The dotted line indicates the position of the host valence band maximum, and the dash line gives the position of the highest occupied state.

s around the TM impurity correspond to electronic orbitals with lobes pointing to the interstitial region pointing to the interstitial region for the TM atom in a tetrahedral environment, i.e., to the  $\langle 100 \rangle$  directions for the nonbonding  $e$  orbitals and the  $[11\bar{1}]$   $[\bar{1}11]$   $[1\bar{1}1]$   $[\bar{1}11]$  directions for the antibonding  $t$  orbitals, as shown by their electron densities in Fig. 8. The directional dependence is strong for all the nonbonding orbitals, as well as for the antibonding orbitals for systems with a small TM atomic number  $Z$  (e.g., Cr) and a small anion  $Z$  (e.g., N) due to the level anti-crossing [27, 47, 48]. The spatial extent to the interstitial region is large for the nonbonding orbitals for systems with a small TM  $Z$  (e.g., Ti), as well as for the antibonding orbitals for the nitrides with a small TM  $Z$  (e.g., Cr).

To understand the mechanism for the trends in the spatial extent of the isolated TM-derived orbitals, we investigate the spatial extent of the

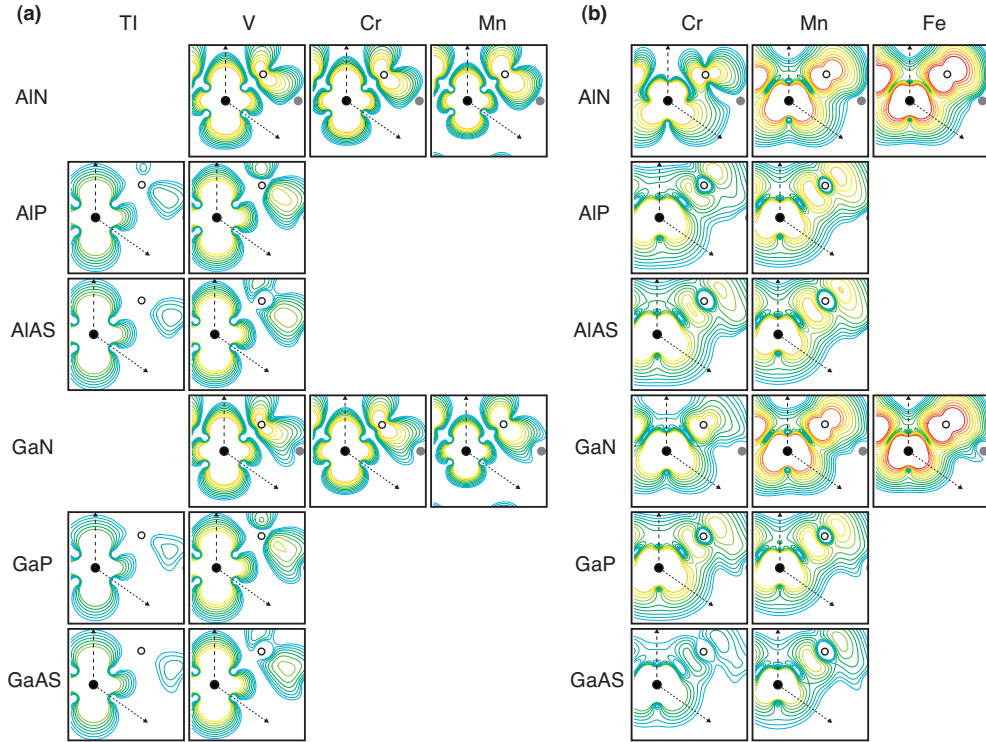


Figure 8: Electron density in the (110) plane of isolated TM impurities. The electron densities due to the occupied (a) nonbonding  $e$  levels and (b) antibonding  $t$  levels in the gap. The black filled, gray filled, and open circles indicate the TM, host cations, and host anions, respectively. The dash and dotted lines indicate the  $[100]$  and  $[11\bar{1}]$  directions, respectively. The contours start from  $0.001 e/\text{\AA}^3$  (cyan), increase by a factor of  $\sqrt{2}$ , and end to  $0.064 e/\text{\AA}^3$  (red).

nonbonding  $e$  and/or antibonding  $t$  levels along the interstitial directions shown by dashed and dotted lines in Fig. 8. To quantify this extent, we evaluate the distance  $l$  from the TM site to the points where the electron density essentially vanishes, i.e., reaches a value of  $10^{-3} e/\text{\AA}^3$ , which is about one hundredth or less of the values observed close to nucleus. We wish to probe how sensitive this extent  $l$  is on the TM-anion hybridization, which can be artificially altered by adiabatically varying the lattice constant  $a$ . The spatial extent  $l$  is plotted against  $a$  in Fig. 9. This spatial extent of the nonbonding orbitals depends on the TM species and is large for systems with a small TM atomic number  $Z$ . This spatial extent of the antibonding orbitals depends on both the TM species and the lattice constant, i.e., the TM-anion bond length, which in turn is correlated with the TM-anion hybridization. The spatial extent

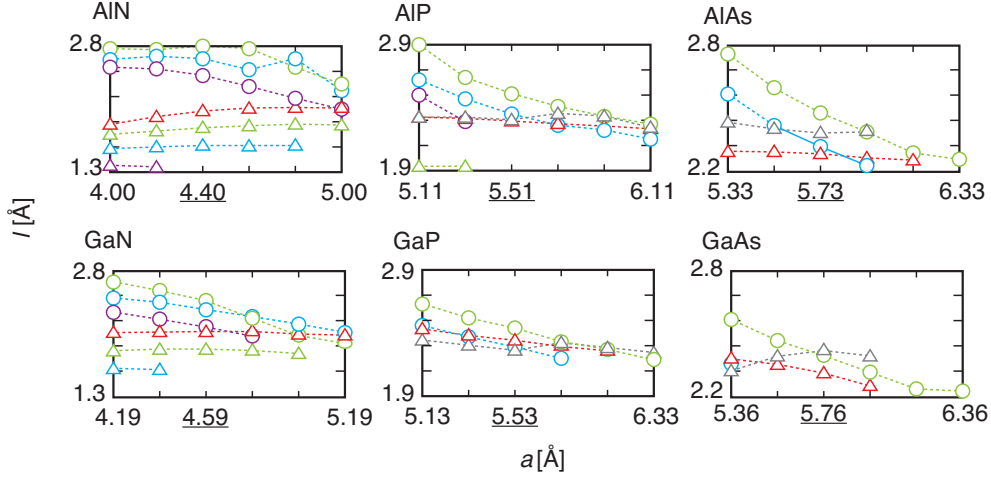


Figure 9: Spatial extent of the isolated TM-derived orbitals from the TM nucleus to the interstitial region. The distance  $l$  from the TM site to the point with the value of the electron density due to the occupied non-(anti-)bonding levels in the gap  $= 10^{-3} e/\text{\AA}^3$  along the  $[100]$  ( $[11\bar{1}]$ ) direction while varying the lattice constant  $a$  (without atomic relaxation). The grey, red, green, blue, and purple colored triangles (circles) indicate the  $d$  for the non-(anti-)bonding gap states for Ti, V, Cr, Mn, and Fe, respectively. The underlined values indicate the calculated equilibrium lattice constant.

of the antibonding orbitals is large for systems with a small TM  $Z$  and a short TM-anion bond length, i.e., systems with strong  $p$ - $d$  interactions [59]. We conclude that the large spatial extent of the nonbonding orbitals for systems with a small TM  $Z$  is due to the weak electron-nucleus Coulomb attraction for a small TM  $Z$ , and that of the antibonding orbitals for the nitrides with a small TM  $Z$  is due to the weak electron-nucleus Coulomb attraction for strong  $p$ - $d$  interactions.

#### 4.4 The charge neutral TM impurity pairs in III-V semiconductors

The nearest neighbor TM pairs in a semiconductor or insulator host induce a manifold of defect levels in the gap as shown by the calculated density of states given in Fig. 10. These levels can be classified as  $e$ - $e$  and/or  $t$ - $t$  levels due to the interaction of two isolated impurity  $e$  or  $t$  levels as introduced in Appendix C.2. The wide energetic range of these levels for Ti, V, Cr, and Mn and the narrow energetic range of these levels for Fe respectively correspond to the ferromagnetic spin configurations

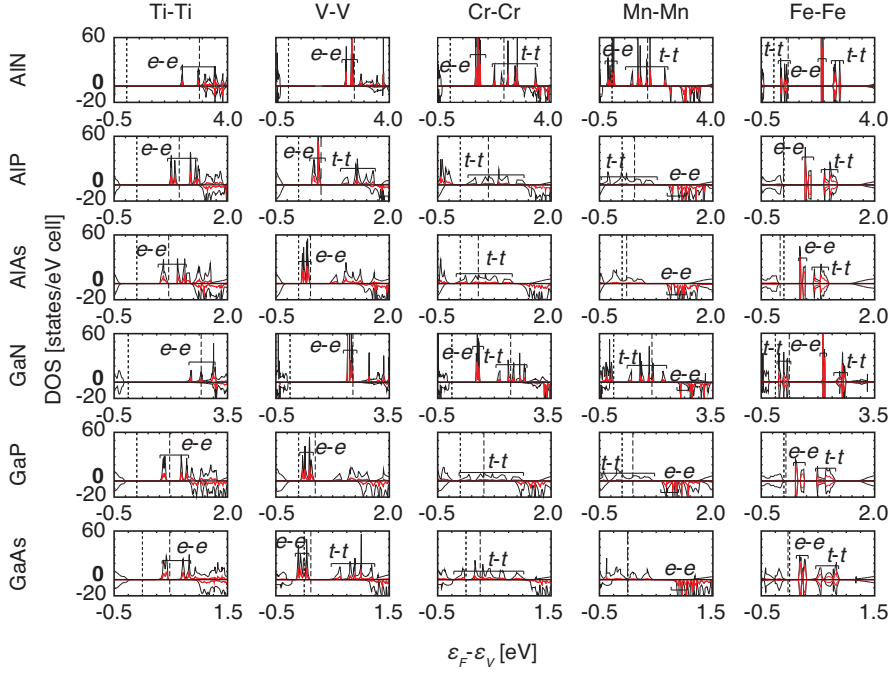


Figure 10: Spin polarised densities of states (DOS) of the nearest neighbor TM impurity pairs. The black and red lines indicate the total DOS and the transition-metal local DOS, respectively. The levels labeled by  $e-e$  ( $t-t$ ) indicate the levels due to the two  $e$  ( $t$ ) levels within the gap. The positive and negative DOS values indicate majority and minority spin DOS, respectively. The dotted line indicates the position of the host valence band maximum, and the dash line gives the position of the highest occupied state.

for Ti, V, Cr, and Mn and the anti-ferromagnetic spin configuration for Fe in the ground states as previously reported in Refs. [45–49, 54].

The electron density distributions corresponding to these levels are shown in Fig. 13. The pair interactions may further be classified as an interaction due to the overlap of the isolated TM- $d$  orbitals, i.e.,  $d-d$  interactions, or an anion mediated  $p-d$  interaction due to the overlap of TM- $d$  states with host anion states. As seen in Fig. 13, the  $e-e$  levels for Ti and the  $t-t$  levels for the nitrides with Cr show a clear signature of  $d-d$  interactions. These systems exhibit a covalent bond, which is completely different of any superposition of the respective isolated defect electron densities. Such dominant  $d-d$  interactions in the defect pair electron densities are due to the interaction of two isolated TM- $d$  orbitals with both a strong directional dependence to the interstitial region and a large spatial extent to the region.

The pairwise magnetic and chemical interactions of TM impurities in



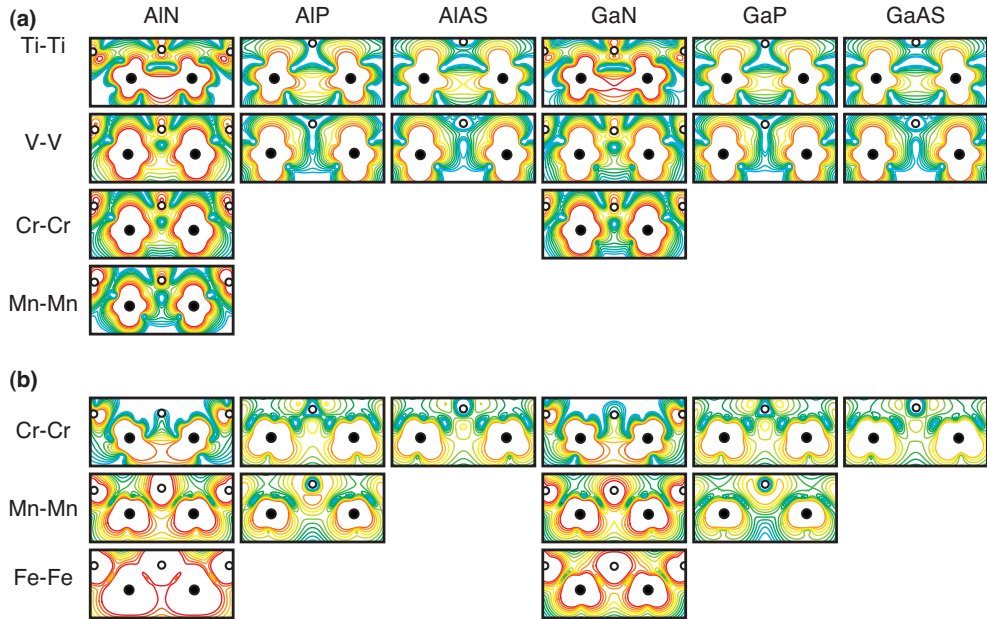


Figure 11: Electron density in the (110) plane of the nearest neighbor TM impurity pairs. The electron densities due to the occupied bands (a) due to the two nonbonding levels (b) due to the two antibonding levels in the gap. Black filled and open circles indicate the TM and anions, respectively. The contours start from  $0.001 e/\text{\AA}^3$  (cyan), increase by a factor of  $\sqrt{2}$ , and end to  $0.064 e/\text{\AA}^3$  (red).

III-V semiconductors can be attributed to the interaction of two nonbonding or antibonding orbitals corresponding to whether the highest occupied states of the isolated TM impurity are nonbonding or antibonding orbitals [27, 28, 45–49, 54]. Therefore, we conclude that these pairwise interactions can be defined as *d-d* interactions for systems with a small TM atomic number  $Z$  where the highest occupied states of the isolated TM impurity are nonbonding orbitals (e.g., Ti in III-V semiconductors) and systems with a small TM  $Z$ , small anion  $Z$ , and short TM-anion bond length where the highest occupied states are antibonding states (e.g., Cr in III-N semiconductors).

## 4.5 Summary

In this chapter, the pairwise magnetic and chemical interactions of a range of transition metal (TM) impurities in various III-V semiconductors for a charge neutral condition are theoretically studied. The main

result is that these pairwise interactions can be defined as  $d-d$  interactions for systems that fulfill the following criteria:

- a small TM atomic number  $Z$  where the highest occupied states of the isolated TM impurity are nonbonding orbitals (e.g., Ti in III-V semiconductors),
- a small TM  $Z$ , a small anion  $Z$ , and a short TM-anion bond length where the highest occupied states are antibonding states (e.g., Cr in III-N semiconductors).

These criteria allow us to discriminate between  $d-d$  interactions or the  $p-d$  hybridization based on a calculation of only the isolated impurity.

In Chapters 3 and 4, charge state of TM impurities are limited to a charge neutral state. TM impurities, however, exhibit various charged states depending on the external doping conditions. For the sake of generality, we investigate the pairwise chemical interaction of a range of TM impurity pairs in various insulators for various charged conditions as introduced in the next chapter.

## 5 The charged TM impurities in insulators

Exotic magnetic properties of transition metal (TM) doped semiconductors or insulators are intimately connected with TM clustering [4, 40, 60, 61]. TM clustering may be predicted starting from the pairwise chemical interaction among the TM impurities. We have recently shown that in addition to the well-known  $p$ - $d$  hybridization [46, 62] and Coulomb interactions [61, 63], direct  $d$ - $d$  interactions [54, 55, 64] can play a crucial role in the description of pairwise magnetic and chemical interactions. Thus far, however, such  $d$ - $d$  interactions have only been studied for charge neutral impurities, which leaves open the question of how these  $d$ - $d$  interactions change when system charges are altered. We report a systematic theoretical study of the pairwise chemical interaction and  $d$ - $d$  interactions in various insulators for various charged conditions using *ab initio* methods.

This chapter is structured as follows. The computation details are introduced in Section 5.1. Structural parameters of bulk insulators are discussed in Section 5.2. The electronic structure of isolated charged TM impurities in insulators is discussed in Section 5.3. The magnetic and chemical interactions of the charged TM impurity pairs in insulators are discussed in Section 5.4. Finally, we sum up all results and draw a conclusion in Section 5.5.

### 5.1 Computational details

We consider several insulators of MgO, AlN, GaN, GaAs, ZnTe, and CdTe with an isolated TM impurity and the respective nearest neighbor pair. For TM we consider Cr, Mn, Fe. We carry out total energy calculations within generalized gradient approximation (GGA-PBE) [12] to the density-functional theory together with projector augmented wave methods [14], as implemented in the VASP package [32, 33]. The MgO is modeled with rocksalt-structured supercells of 64 atoms and the others are modeled with zincblende-structured supercells of 64 atoms, with one or two cations replaced by a TM atom, representing the isolated impurity and nearest-neighbor pair, respectively. The plane-wave cutoff is set at 460 eV, 460 eV, 460 eV, 290 eV, 290 eV, and 290 eV for MgO(:TM), AlN(:TM), GaN(:TM), GaAs(:TM), ZnTe(:TM), and CdTe(:TM), respectively.  $k$ -point meshes is set at  $3 \times 3 \times 3$ ,  $3 \times 3 \times 3$ ,  $3 \times 3 \times 3$ ,  $3 \times 3 \times 3$ ,  $2 \times 2 \times 2$ , and  $3 \times 3 \times 3$  for MgO(:TM), AlN(:TM), GaN(:TM), GaAs(:TM), ZnTe(:TM), and CdTe(:TM), respectively. These parameters are determined as described in Appendix B.2. The total energies in the system charge  $q \neq 0$  are modified for image charges in the finite supercell method

together with proper potential alignment, as described in Ref. [58].

## 5.2 Bulk insulators

The equilibrium lattice constant of bulk insulators were computed and compared to experiment and previous theory as given in Table 6. The agreement with experimental and theoretical data is very good, with deviations from experiment below 3% and theory below 1%.

Table 6: Calculated lattice constants with experiment for the pure host.

System	PBE (present) [Å]	PBE(Refs [56])	Expt. [Å] [57]
MgO	4.24	4.260	4.212
AlN	4.40	4.402	4.36
GaN	4.59	4.546	4.50
GaAs	5.76	5.752	5.653
ZnTe	6.19	6.194	6.10
CdTe	6.63	6.624	6.48

## 5.3 Isolated charged TM impurities in insulators

An isolated TM impurity in a semiconductor or insulator host induces defect levels in the forbidden band gap of the host that may introduce or trap carriers (electrons or holes). The defect levels for the TM atom in a tetrahedral or octahedral environment can be classified into  $e$  and/or  $t_2$  represented levels from the projection of the TM local density of states onto the  $e$  and  $t_2$  representations. Note however that, the minority spin  $e$  state of the tellurides with Mn in  $q=-1$  falsely strongly hybridize with the conduction band due to LDA (GGA) errors [27, 58], and thus, are not considered henceforth.

The TM induced levels can be described as non-bonding and/or anti-bonding levels in the gap due to  $p-d$  (anion-TM) interactions as introduced in Appendix C.1. The non-bonding and anti-bonding states around the TM atom and the first nearest anions can be visualized by their electron densities in Fig. 12. For increasing the system charge, the spatial extent of these states increase mainly around the TM atom due to a decrease in electron-nucleus Coulomb attraction for a decrease in TM oxidation numbers.

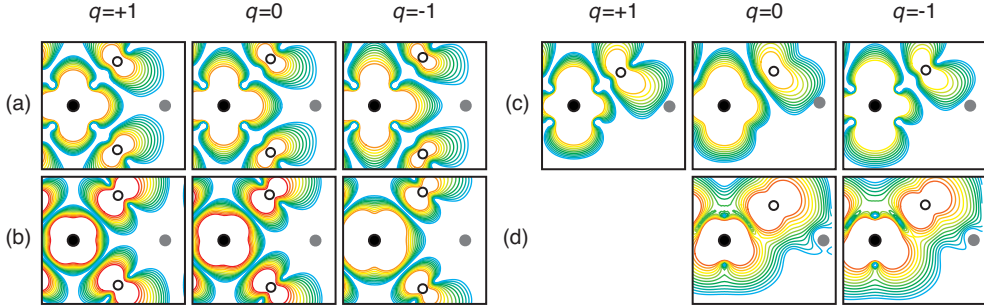


Figure 12: Electron density of isolated TM impurities. The electron densities in the (100) plane due to (a) the triply occupied nonbonding  $t$  levels in the gap for MgO:Cr and (b) doubly occupied antibonding  $e$  levels in the gap for MgO:Fe. The electron densities in the (110) plane due to (c) the doubly occupied nonbonding  $e$  levels in the gap for AlN:Cr and (d) triply occupied antibonding  $t$  levels in the gap for GaN:Fe. The black filled, gray filled, and open circles indicate the TM, host cations, and host anions, respectively. The contours start from  $0.001 e/\text{\AA}^3$  (cyan), increase by a factor of  $\sqrt{2}$ , and end to  $0.064 e/\text{\AA}^3$  (red).

## 5.4 The charged TM impurity pairs in insulators

The nearest neighbor TM pairs in a semiconductor or insulator host induce a manifold of defect levels in the gap. These levels can be roughly classified as  $e-e$  and/or  $t-t$  levels due to the interaction of two isolated impurity  $e$  or  $t$  levels as introduced in Appendix C.2. Note however that, the anti-bonding  $e-e$  states of the tellurides with Mn in  $q=-1$  and  $q=-2$  falsely strongly hybridize with the conduction band due to LDA (GGA) errors [27, 58], and thus, are not considered henceforth.

The electron density distributions corresponding to these levels are shown in Fig. 13. For increasing the system charge, the degree of the direct TM-TM electron density overlap, which is a testimony of  $d(\text{TM})-d(\text{TM})$  interactions, increases corresponding to the increase in the spatial extent of the TM-derived states around the TM atoms except for systems where  $d-d$  interactions can be expected to be trivial [64] (e.g., CdTe:Cr). For the systems, the degree of the density overlap reaches to the maximum around the system charge  $q=0$ .

To see the relation between the TM-TM density overlap and the TM-TM distance, we show the TM-TM distance in Fig. 14. For increasing the system charge, the contraction of the TM-TM distance as compared to the distance between the host cations goes to be enhanced except for systems where  $d-d$  interactions can be expected to be trivial [64] (e.g., C

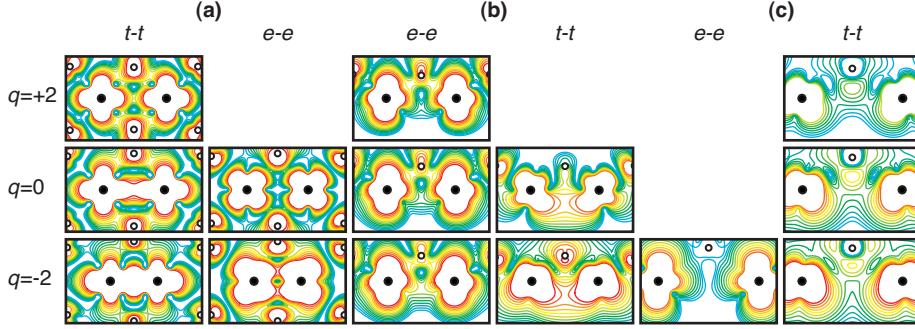


Figure 13: Electron density of the nearest neighbor TM impurity pairs. The electron densities in the (100) plane due to the occupied levels due to the two nonbonding  $t$  (antibonding  $e$ ) levels in the gap (a) for MgO:Cr-Cr. The electron densities in the (110) plane due to the occupied levels due to the two nonbonding  $e$  (antibonding  $t$ ) levels in the gap (b) for GaN:Cr-Cr and (c) for CdTe:Cr-Cr. Black filled and open circles indicate the TM and anions, respectively. The contours start from  $0.001 e/\text{\AA}^3$  (cyan), increase by a factor of  $\sqrt{2}$ , and end to  $0.064 e/\text{\AA}^3$  (red).

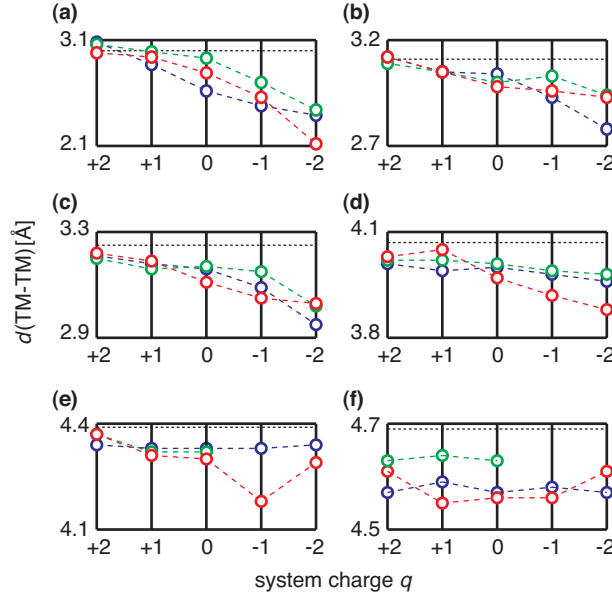


Figure 14: Distances between the TM atoms for the nearest neighbor TM impurity pairs. For (a) MgO, (b) AlN, (c) GaN, (d) GaAs, (e) ZnTe, (f) CdTe. The red, green, and blue circles indicate Cr, Mn, and Fe, respectively. The horizontal dotted line indicate the distances between the host cations.

(e.g., dTe:Cr). For the systems, the contraction reaches to the maximum

around the system charge  $q=0$ . This trend in the contraction of the TM-TM distance is consistent with the trend in the increase of the degree of the TM-TM electron density overlap.

Whether impurity pairs are energetically stable or not as compared to two isolated impurities can be evaluated by the binding energy  $E_b$  [55,65] defined as  $E_b = \Delta H[\text{TM} - \text{TM}] - 2\Delta H[\text{TM}]$ , where  $\Delta H_{D,q}(\varepsilon_F, \mu) = (E_{D,q} - E_H) + \sum_{\alpha} n_{\alpha} \mu_{\alpha} + q\varepsilon_F$ . Here  $E_H$  is the energy of the pure host, and  $E_{D,q}$  the energy of a defect containing system.  $\mu_{\alpha}$  is the chemical potential of a reservoir of atoms  $\alpha$ , and the Fermi-level  $\varepsilon_F$  is the chemical potential of the electron reservoir. Negative (positive) values of the binding energy  $E_b$  indicate that a pairs are energetically stable (unstable) as compared to two isolated impurities. To see which of the system charge  $q$  for a pairs and isolated impurities corresponds to the Fermi-level position, we calculate the binding energy  $E_b$  and also the transition energy  $\varepsilon(q', q'')$  i.e., the ionization energy from charge  $q'$  to  $q''$  [39, 55, 65] defined as  $\varepsilon(q'/q'') = \frac{E_{D,q''} - E_{D,q'}}{q' - q''} - \varepsilon_v$ , where  $\varepsilon_v$  is the valence band maximum  $\varepsilon_v$ . The binding energy  $E_b$  and transition energy  $\varepsilon(q', q'')$  of the impurities for various charged conditions are shown in Fig. 15. The energy  $E_b$  incre-

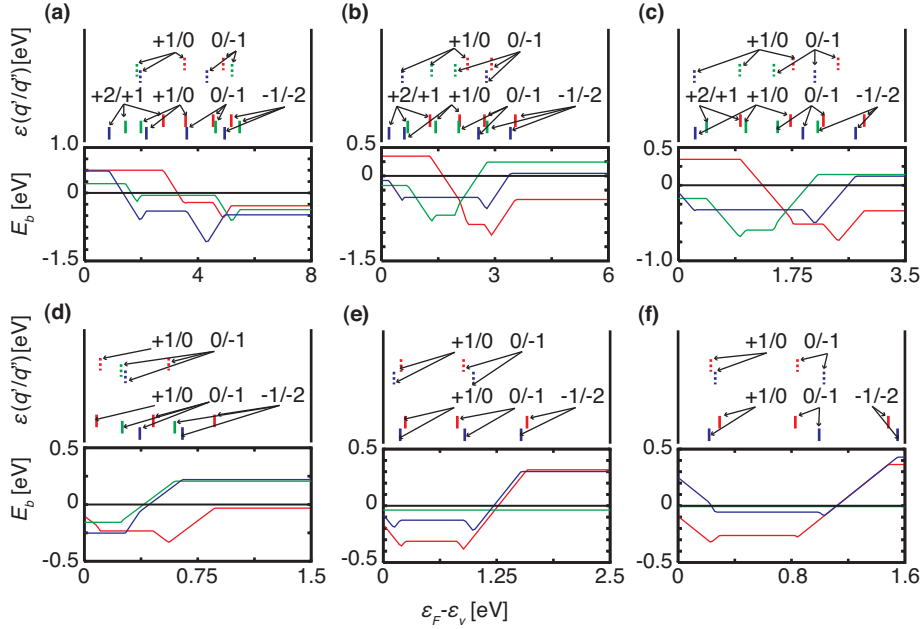


Figure 15: Binding energy  $E_b$  and transition energy  $\varepsilon(q', q'')$ . For (a) MgO, (b) AlN, (c) GaN, (d) GaAs, (e) ZnTe, (f) CdTe. The  $\varepsilon_F$  and  $\varepsilon_v$  indicate the Fermi-level and valence band maximum. The red, green, and blue lines indicate the  $E_b$  and  $\varepsilon(q', q'')$  for Cr, Mn, and Fe, respectively.

ases for increasing the system charge for MgO:TM, and for the others the energy  $E_b$  reaches to the maximum around the system charge  $q=0$ . The trend for MgO:TM cannot be described due to Coulomb interactions [61, 63]. These trends in the binding energy consistent with the contractive trend in the TM-TM distance and the increasing trend in the degree of the TM-TM electron density overlap only for MgO:TM.

## 5.5 Summary

In this chapter, the pairwise chemical interaction and  $d-d$  interactions of a range of transition metal (TM) impurities in various insulators for various charged conditions are theoretically studied. The main results is that only for the system with the smallest anion  $Z$  and the shortest lattice constant the trend in the pairwise chemical interaction for various charged conditions can be attributed to the trend in  $d-d$  interactions. This indicates that  $d-d$  interactions are not always a sufficient quantity to describe the pairwise chemical interaction.



## 6 Summary and outlook

Diluted magnetic semiconductors (DMSs) are promising candidates for novel spintronics materials, as some of DMSs show novel magnetic properties. Recent study on DMSs has revealed that magnetic properties of DMSs are intimately connected with transition metal (TM) cluster formation. For clarifying the relation between the magnetic properties and TM cluster formation, understanding the pairwise magnetic and chemical interactions of TM impurities in semiconductors is a minimum requirement. These pairwise interactions have been studied over the past few decades, and for the mechanisms of these pairwise interactions, several phenomenological models have been presented. However, these pictures can only partially capture trends in these pairwise interactions and have not even given a congruous view of these pairwise interactions for the very same materials.

In this thesis, detailed theoretical studies of these pairwise interactions are presented. The first part of the thesis (Chapter 3) focuses on the investigations of these pairwise interactions of Cr impurities in AlN for a charge neutral condition. We find a strong ferromagnetic interaction that can not be described with conventional magnetic interaction models and a strong attractive chemical interaction for the Cr pairs, which can be described mainly due to  $d-d$  interactions. The second part of the thesis (Chapter 4) focuses on the investigations of these pairwise interactions of TM impurities in III-V semiconductors for a charge neutral condition. We find that  $d-d$  interactions that are usually assumed to be negligible always appear to some extent for the TM pairs and become particularly important in the description of pairwise magnetic and chemical interactions for light  $3d$  transition metal impurities in nitride semiconductors. This finding is consistent with our finding summarized in the first part of the thesis (Chapter 3). The final part of the thesis (Chapter 5) focuses on the investigations of the pairwise chemical interaction of TM impurities in insulators for various charged conditions. We show that only for the system with the smallest anion atomic number  $Z$  and the shortest lattice constant the trend in the pairwise chemical interaction for various charged conditions can be attributed to the trend in  $d-d$  interactions. This indicates that  $d-d$  interactions are not always a sufficient quantity to describe the pairwise chemical interaction.

A large part of my PhD work has been dedicated to understanding the magnetic and chemical interactions of the nearest neighbor substitutional TM impurity pairs in semiconductors in detail. The detailed understanding of such short-range interactions does not directly allow us

to understand the properties of TM impurities in semiconductors. However, the detailed understanding of such short-range interactions will be important when one use design principles [61, 65, 66] to obtain target magnetic properties via controlling TM cluster formation for DMSs.

# Appendices

# A Models for the pairwise magnetic interaction

## A.1 Open shell models

”Open shell” models are constructed to describe ferromagnetic interactions of transition metal (TM) compounds for the existence of partial occupancies in the electronic states of the isolated TM atom [25–28]. The models can be classified into double exchange model [25, 26] or  $p$ - $d$  hopping model [27, 28], whether the models are described in the electronic picture or hole picture. In either models, the magnetic interaction is described via the  $p$ (anion)- $d$ (TM) hybridization. The hybridization yields bonding and antibonding levels in the each spin channel. In the case of the existence of partial occupancies in the electronic states, occupancies of bonding levels are more than those of antibonding levels for one spin channel, which yields energy gain for parallel spin configurations (i.e., ferromagnetic interaction) as seen in Fig. 16 (a). In the case of the absence of partial occupancies in the electronic states, both bonding and antibonding levels for one spin channel are completely filled, which does not yield energy gain for parallel spin configurations (i.e., non-ferromagnetic interaction) as seen in Fig. 16 (b).

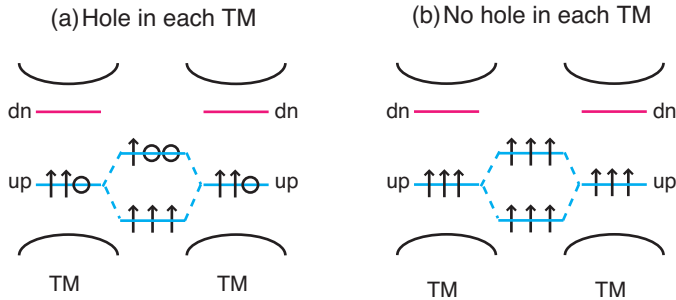


Figure 16: Schematic energy levels of two interacting TM for parallel spin configurations in the case of (a) existence and (b) absence of partial occupancies in the isolated TM derived electronic states for TM compounds.

## A.2 Superexchange models

Superexchange models are constructed to describe antiferromagnetic interactions of TM compounds for the absence of partial occupancies in the electronic states of the isolated TM atom [29], under special circumstances the models can yield ferromagnetic interactions without the

partial occupancies [30,31]. Here, the magnetic interactions are described via the  $p(\text{anion})$ - $d(\text{TM})$  hybridization. The hybridization between occupied  $p$  orbital of anion and occupied  $d$  orbital of TM atom can only take place by donation of electron from anion atom into the vacant  $d$  states of the TM atom whose spin state is opposite to the spin state of the electron of anion atom. On the contrary, the hybridization between occupied  $p$  orbital of anion and vacant  $d$  orbital of TM atom can only take place by donation of electron from anion atom into the vacant  $d$  states of the TM atom whose spin state is the same as the spin state of the electron of anion atom in order to optimize Hund's rule coupling to the TM atom. Then superexchange yields anti-ferromagnetic interactions for the case in Fig.17 (a) and Fig. 17 (b) and ferromagnetic interactions for the case in Fig.17 (c) and Fig. 17 (d).

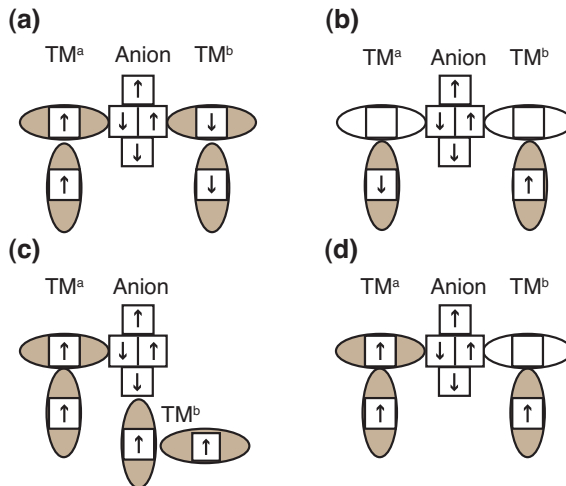


Figure 17: Superexchange for two TM atoms separated by an anion. Anti-ferromagnetic interactions for non-orthogonally arranged TM pairs (a) where both TM<sup>a</sup>-anion and TM<sup>b</sup>-anion bonds are covalent. (b) where both TM<sup>a</sup>-anion and TM<sup>b</sup>-anion bonds are ionic. Ferromagnetic interactions (c) for orthogonally arranged TM pairs where both TM<sup>a</sup>-anion and TM<sup>b</sup>-anion bonds are covalent and (d) for non-orthogonally arranged TM pairs where one of TM<sup>a</sup>-anion and TM<sup>b</sup>-anion is ionic.

## B Way to determine parameters

### B.1 $U$ and $J$ parameters

In  $+U$  calculations, there are some ways to choose  $U$  and  $J$  parameters [67–69]. Here, we use Lany *et al.* approach [69], where  $(U - J)$

parameters are chosen to recover the error coming from the limitation of LDA or GGA about thermochemical phase stability of the different oxide stoichiometries (e.g, NiO and Ni<sub>2</sub>O<sub>3</sub>).

For the Cr impurity, we choose  $U$  parameters with  $J$  parameters of 1.0 eV, to reproduce the correct thermochemical stability of CrO<sub>2</sub> and Cr<sub>2</sub>O<sub>3</sub>. In thermodynamic equilibrium, the Cr and oxygen chemical potentials must satisfy the stability condition for CrO<sub>2</sub> and Cr<sub>2</sub>O<sub>3</sub>; Eq.(A):  $\Delta\mu_{\text{Cr}} + 2\Delta\mu_{\text{O}} = \Delta H_f(\text{CrO}_2)$  and Eq.(B):  $2\Delta\mu_{\text{Cr}} + 3\Delta\mu_{\text{O}} = \Delta H_f(\text{Cr}_2\text{O}_3)$ , where  $\Delta H_f$  is the calculated CrO<sub>2</sub> and Cr<sub>2</sub>O<sub>3</sub> formation enthalpy.  $\Delta\mu_{\text{O}}$  versus  $\Delta\mu_{\text{Cr}}$  for CrO<sub>2</sub> and Cr<sub>2</sub>O<sub>3</sub> for both the experiments [57] and GGA calculations is plotted in Fig. 18. At  $\Delta\mu_{\text{O}} \sim -0.6$  eV, experimental data suggests Cr<sub>2</sub>O<sub>3</sub> is stable with respect to CrO<sub>2</sub>, but GGA calculation does Cr<sub>2</sub>O<sub>3</sub> is unstable with respect to CrO<sub>2</sub>. We thus determine  $U$  parameters with  $J$  parameters of 1.0 eV, as in the GGA+ $U$  calculations Cr<sub>2</sub>O<sub>3</sub> is stable with respect to CrO<sub>2</sub> at  $\Delta\mu_{\text{O}} \sim -0.6$  eV simply increasing  $U$  parameters with  $J$  parameters of 1.0 eV. We obtain  $U$  parameters as 3.0 eV with  $J$  parameters of 1.0 eV.

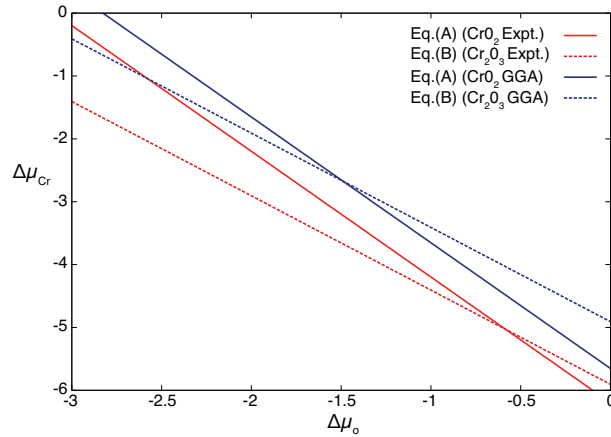


Figure 18:  $\Delta\mu_{\text{O}}$  versus  $\Delta\mu_{\text{Cr}}$  for CrO<sub>2</sub> and Cr<sub>2</sub>O<sub>3</sub> for both the experiments and GGA calculations.

## B.2 Cutoff energy and $\vec{k}$ -point meshes

For calculating total energies and electronic structures of systems, we need parameters of the cutoff energy  $E_{\text{cut}}$  and  $\vec{k}$ -point meshes. The Kohn-Sham wave functions in the Bloch states are expressed by using a plane wave expansion

$$\varphi_{\mathbf{k},i}(\mathbf{r}) = \sum_{\mathbf{G}} c_{\mathbf{k},i}^{\sigma} e^{i(\mathbf{k}+\mathbf{G})\cdot\mathbf{r}}, \quad (29)$$

where  $\mathbf{k}$  is a wave vector in the first Brillouin zone (BZ) that is the volume within the boundary that define the condition for Bragg reflection, and  $\mathbf{G}$  is reciprocal lattice vectors concerned with the real space lattice vectors as shown in the following equation  $e^{i\mathbf{G}\cdot\mathbf{R}} = 1$ , where  $\mathbf{R}$  is the real space lattice vectors. In practical calculations, the Fourier expansion of the wave functions (in equation (29)) is truncated by keeping only those plane wave vectors with a kinetic energy  $(\vec{k} + \vec{G})^2/2$  lower than a given cutoff value  $E_{\text{cut}}$

$$\frac{1}{2}(\vec{k} + \vec{G})^2 < E_{\text{cut}}. \quad (30)$$

The convergence of all calculations with respect to the basis set size should be tested simply by increasing step by step the plane wave cutoff energy  $E_{\text{cut}}$ .

Physical quantities like the electron density can be evaluated by integration over  $\vec{k}$  inside only the first Brillouin zone (BZ). This is because any  $k'$  not in the first BZ can be expressed  $\vec{k}' = \vec{k} + \vec{G}$ , where  $\vec{k}$  lies in the first BZ, when the eigenstates are in the Bloch states. In practical calculations, we replace the integration over the BZ by a discrete weighted sum over a chosen  $\vec{k}$ -point meshes. For a chosen  $\vec{k}$ -point meshes, we use a  $\Gamma$ -centered Monkhorst-Pack scheme [70]. In Monkhorst-Pack method, the  $\vec{k}$ -point meshes are defined using three integers  $(L, M, N)$ , and the  $(L \times M \times N)$  points are spaced evenly along the reciprocal lattice vectors in the first BZ. For increasing size of the supercell, the volume of the Brillouin zone becomes smaller and smaller (from  $e^{i\vec{G}\cdot\vec{R}}$ ). With increasing supercell size more and more, less and less  $\vec{k}$ -points are therefore needed. Ideally, high cut off energy and condensed  $\vec{k}$ -point meshes are needed, but the calculations become impractical. We thus need to determine finite values for these parameters which can yield sufficient accuracy.

In order to obtain such parameters in large (64~96) atom supercells that are used for the transition metal (TM) doped materials studied in this thesis, we carry out convergence tests for cutoff energy and  $\vec{k}$ -point meshes in small ( $\sim 8$ ) atom supercells for the host materials. In the convergence test for the cutoff energy, the relative energies between systems

with different lattice constant under the same  $\vec{k}$ -point meshes were found to converge to a precision of roughly 1 meV. In the convergence test for the  $\vec{k}$ -point meshes, the relative energies between systems with different lattice constant under the same cutoff energy were found to converge to a precision of roughly 1 meV. Whenever we use different size of supercells, we scale the  $\vec{k}$ -point meshes according to the lengths of the reciprocal lattice vectors as the dense of the  $k$ -point meshes becomes same as the dense of  $\vec{k}$ -point meshes in the small atom supercells.

## C Description of defect levels in the band gap of TM impurities

### C.1 An isolated TM impurity

The formation of a substitutional transition metal impurity can be thought of as a two step process, involving first the removal of a host cation atom, and second, the placement of a transition metal (TM) impurity atom in its place [71]. The removal of a cation atom creates anion atoms surrounding the cation atom dangling bonds. The placement of a TM impurity atom in its place yields nonbonding and/or antibonding levels in the gap region due to the interaction of the TM's symmetry-adapted  $3d$  levels and the anion dangling bonds that have the same representation as the symmetry-adapted  $3d$  levels. The spatial distribution of the antibonding states changes when the system's TM and anion are altered [47, 48]. For the systems with large  $Z$  TM and large  $Z$  anion, the antibonding states become  $p$ -orbital like levels as shown in Fig. 19 (a). For the systems with small atomic number  $Z$  TM and small  $Z$  anion, the antibonding states become  $d$ -orbital like levels as shown in Fig. 19 (b). The similar interchange in a  $d$  character and  $p$  character of the antibonding states are expected when the system charge is altered [39]. When the system charge is increased, the TM- $d$  levels are higher in energy than the anion  $p$ -levels, which increases a  $d$  character and reduce a  $p$  character in the antibonding states as shown in Fig. 19 (a)  $\rightarrow$  Fig. 19 (b).



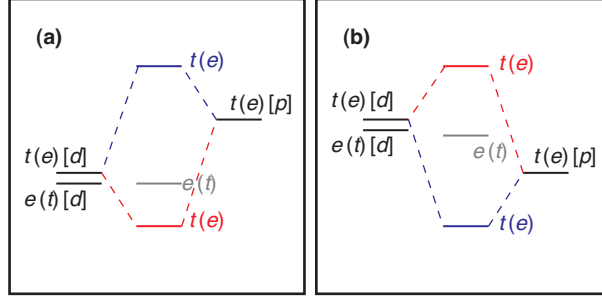


Figure 19: Schematic energy-level diagram of an isolated TM impurity in a tetrahedral (octahedral) semiconductor or insulator (a) for the system with large atomic number  $Z$  TM and large  $Z$  anion or the system with less system charge (b) for the system with small  $Z$  TM and small  $Z$  anion or the system with more system charge. In each panel, the mixed levels (center) are generated from the interaction between crystal-field levels on the TM- $d$  (left) with the anion- $p$  levels (right).

## C.2 TM impurity pairs

For the nearest neighbor TM pairs in a semiconductor or insulator host, defect levels in the gap are usually described due to the interaction of two isolated impurity nonbonding or antibonding levels as illustrated in Fig. 20. We however observe an exception to this picture for the "out-of-plane" configurations for Cr doped AlN as discussed in section 3.4 which may be due to very strong polarization effects of AlN as discussed in Ref. [72].

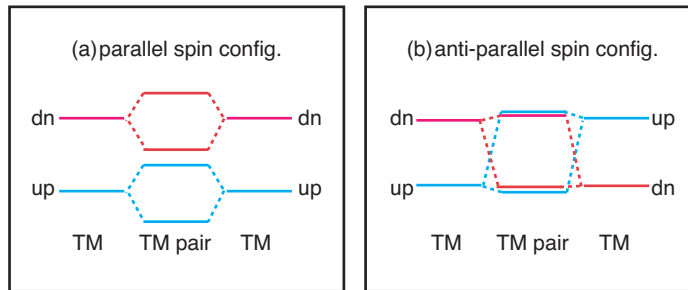


Figure 20: Schematic energy-level diagram of the nearest neighbor TM impurity pairs (a) for parallel spin configuration and (b) anti-parallel spin configuration. The up (dn) indicates majority (minority) spin states. In each panel, the mixed levels (center) are generated from the interaction between the isolated TM-derived levels (left and right).

## D Finite-size effects due to charged defects

Supercell approach describes efficiently and accurately the crucial local rearrangements of bonding between atoms, it also introduces artificial long-range interactions between the periodic defect images. In this approach, total energies are evaluated by setting the divergent terms of the electron-ion potential  $V_{ei}(G=0)$ , Hartree potential  $V_H(G=0)$ , and ion-ion potential  $V_{ii}(G=0)$  to zero. In the charge-neutral case, this procedure is justified by the exact cancellation of the respective terms [73–75]. In the charged calculation, the omission of the averaged electrostatic potential can be viewed as an effective compensation for the net charge by a homogeneous jellium background charge and virtually yield the jellium-defect and defect-defect interactions. For the correction for the jellium-defect interaction, we use Lany *et al.* approach [58] as

$$\Delta E_{\text{pa}}(D, q) = q(V_{D,q}^r - V_H^r), \quad (31)$$

where the reference potentials  $V^r$  in the charged-defect ( $D, q$ ) and pure-host (H) calculations are determined from the local atomic-sphere-averaged electrostatic potentials at atomic sites farther away from the defect. For the correction for the defect-defect interaction, we use Lany *et al.* approach [58] that is practically same as Makov and Payne approach [76] under the conditions of (i) the dielectric constant  $\varepsilon$  is sufficiently large ( $\varepsilon \gg 1$ ) and (ii) the supercell is approximately isotropic as

$$\Delta E_i(V^{1/3}, q) = + \frac{q^2 \alpha_M}{3\varepsilon V^{1/3}}, \quad (32)$$

where  $V$  is the supercell volume and  $\alpha_M$  is the (supercell) lattice-dependent Madelung constant.

## References

- [1] H. Ohno, Making Nonmagnetic Semiconductors Ferromagnetic, *Science* **281**, 951–956 (1998).
- [2] Y. Matsumoto, Room-Temperature Ferromagnetism in Transparent Transition Metal-Doped Titanium Dioxide, *Science* **291**, 854–856 (2001).
- [3] M. Schilfgaarde and O. Mryasov, Anomalous exchange interactions in III-V dilute magnetic semiconductors, *Phys. Rev. B* **63**, 233205 (2001).
- [4] T. Dietl, A ten-year perspective on dilute magnetic semiconductors and oxides., *Nature Mater.* **9**, 965–974 (2010).
- [5] L. R. Velle, *New Topics in Condensed Matter Research*, Nova Science Pub Inc.
- [6] P. Mahadevan and A. Zunger, Ferromagnetism in Mn-doped GaAs due to substitutional-interstitial complexes, *Phys. Rev. B* **68**, 075202 (2003).
- [7] R. E. Behringer, Number of Single, Double, and Triple Clusters in a System Containing Two Types of Atoms, *J. Chem. Phys.* **29**, 537 (1958).
- [8] P. Hohenberg and W. Kohn, Inhomogeneous Electron Gas, *Phys. Rev.* **136**, B864–B871 (1964).
- [9] M. Levy, Universal variational functionals of electron densities, first-order density matrices, and natural spin-orbitals and solution of the  $v$ -representability problem, *Proc. Natl. Acad. Sci.* **76**, 6062–6065 (1979).
- [10] E. H. Lieb, Density functionals for coulomb systems, *Int. J. Quantum Chem.* **24**, 243–277 (1983).
- [11] W. Kohn and L. J. Sham, Self-Consistent Equations Including Exchange and Correlation Effects, *Phys. Rev.* **140**, A1133–A1138 (1965).
- [12] J. P. Perdew, K. Burke, and M. Ernzerhof, Generalized Gradient Approximation Made Simple [*Phys. Rev. Lett.* **77**, 3865 (1996)], *Phys. Rev. Lett.* **78**, 1396–1396 (1997).

- [13] S. L. Dudarev, S. Y. Savrasov, C. J. Humphreys, and A. P. Sutton, Electron-energy-loss spectra and the structural stability of nickel oxide: An LSDA+U study, *Phys. Rev. B* **57**, 1505–1509 (1998).
- [14] P. E. Blöchl, Projector augmented-wave method, *Phys. Rev. B* **50**, 17953–17979 (1994).
- [15] D. Kumar, J. Antifakos, M. G. Blamire, and Z. H. Barber, High Curie temperatures in ferromagnetic Cr-doped AlN thin films, *Appl. Phys. Lett.* **84**, 5004 (2004).
- [16] L. Gu, S. Y. Wu, H. Liu, R. Singh, N. Newman, and D. J. Smith, Characterization of Al(Cr)N and Ga(Cr)N dilute magnetic semiconductors, *J. Magn. Magn. Mater.* **290**, 1395–1397 (2005).
- [17] S. Y. Wu, H. X. Liu, L. Gu, R. K. Singh, L. Budd, M. van Schilf-gaarde, M. R. McCartney, D. J. Smith, and N. Newman, Synthesis, characterization, and modeling of high quality ferromagnetic Cr-doped AlN thin films, *Appl. Phys. Lett.* **82**, 3047 (2003).
- [18] R. M. Frazier, G. T. Thaler, J. Y. Liefer, J. K. Hite, B. P. Gila, C. R. Abernathy, and S. J. Pearton, Role of growth conditions on magnetic properties of AlCrN grown by molecular beam epitaxy, *Appl. Phys. Lett.* **86**, 052101 (2005).
- [19] A. Y. Polyakov, N. B. Smirnov, A. V. Govorkov, R. M. Frazier, J. Y. Liefer, G. T. Thaler, C. R. Abernathy, S. J. Pearton, and J. M. Zavada, Properties of highly Cr-doped AlN, *Appl. Phys. Lett.* **85**, 4067 (2004).
- [20] H. X. Liu, S. Y. Wu, R. K. Singh, L. Gu, D. J. Smith, N. Newman, N. R. Dilley, L. Montes, and M. B. Simmonds, Observation of ferromagnetism above 900 K in Cr-GaN and Cr-AlN, *Appl. Phys. Lett.* **85**, 4076 (2004).
- [21] S. G. Yang, A. B. Pakhomov, S. T. Hung, and C. Y. Wong, Room-temperature magnetism in Cr-doped AlN semiconductor films, *Appl. Phys. Lett.* **81**, 2418 (2002).
- [22] R. Frazier, G. Thaler, M. Overberg, B. Gila, C. R. Abernathy, and S. J. Pearton, Indication of hysteresis in AlMnN, *Appl. Phys. Lett.* **83**, 1758 (2003).

- [23] Y. Endo, T. Sato, A. Takita, Y. Kawamura, and M. Yamamoto, Magnetic, electrical properties, and structure of Cr-AlN and Mn-AlN thin films grown on Si substrates, *IEEE Trans. Magn.* **41**, 2718–2720 (2005).
- [24] Y. Endo, T. Sato, Y. Kawamura, and M. Yamamoto, Crystal Structure and Magnetic Properties of Cr-Doped AlN Films with Various Cr Concentrations, *MATERIALS TRANSACTIONS* **48**, 465–470 (2007).
- [25] C. Zener, Interaction between the d-Shells in the Transition Metals. II. Ferromagnetic Compounds of Manganese with Perovskite Structure, *Phys. Rev.* **82**, 403–405 (1951).
- [26] P. W. Anderson, Considerations on Double Exchange, *Phys. Rev.* **100**, 675–681 (1955).
- [27] A. Zunger, S. Lany, and H. Raebiger, The quest for dilute ferromagnetism in semiconductors: Guides and misguides by theory, *Physics* **3**, 53 (2010).
- [28] P. Mahadevan, A. Zunger, and D. Sarma, Unusual Directional Dependence of Exchange Energies in GaAs Diluted with Mn: Is the RKKY Description Relevant?, *Phys. Rev. Lett.* **93**, 177201 (2004).
- [29] P. Anderson, Antiferromagnetism. Theory of Superexchange Interaction, *Phys. Rev.* **79**, 350–356 (1950).
- [30] J. B. Goodenough, Theory of the Role of Covalence in the Perovskite-Type Manganites [La, M(II)]MnO<sub>3</sub>, *Phys. Rev.* **100**, 564–573 (1955).
- [31] J. Kanamori, Superexchange interaction and symmetry properties of electron orbitals, *J. Phys. Chem. Solids* **10**, 87–98 (1959).
- [32] G. Kresse, From ultrasoft pseudopotentials to the projector augmented-wave method, *Phys. Rev. B* **59**, 1758–1775 (1999).
- [33] G. Kresse, Efficient iterative schemes for ab initio total-energy calculations using a plane-wave basis set, *Phys. Rev. B* **54**, 11169–11186 (1996).
- [34] H. Schulz and K. Thiemann, Crystal structure refinement of AlN and GaN, *Solid State Commun.* **23**, 815–819 (1977).

- [35] K. Miwa and A. Fukumoto, First-principles calculation of the structural, electronic, and vibrational properties of gallium nitride and aluminum nitride, *Phys. Rev. B* **48**, 7897–7902 (1993).
- [36] A. Zoroddu, F. Bernardini, P. Ruggerone, and V. Fiorentini, First-principles prediction of structure, energetics, formation enthalpy, elastic constants, polarization, and piezoelectric constants of AlN, GaN, and InN: Comparison of local and gradient-corrected density-functional theory, *Phys. Rev. B* **64**, 045208 (2001).
- [37] X. Y. Cui, D. Fernandez-Hevia, B. Delley, A. J. Freeman, and C. Stampfl, Embedded clustering in Cr-doped AlN: Evidence for general behavior in dilute magnetic III-nitride semiconductors, *J. Appl. Phys.* **101**, 103917 (2007).
- [38] L.-J. Shi, L.-F. Zhu, Y.-H. Zhao, and B.-G. Liu, Nitrogen defects and ferromagnetism in Cr-doped dilute magnetic semiconductor AlN from first principles, *Phys. Rev. B* **78**, 195206 (2008).
- [39] H. Raebiger, S. Lany, and A. Zunger, Charge self-regulation upon changing the oxidation state of transition metals in insulators., *Nature* **453**, 763–6 (2008).
- [40] H. Ohno, D. Chiba, F. Matsukura, T. Omiya, E. Abe, T. Dietl, Y. Ohno, and K. Ohtani, Electric-field control of ferromagnetism., *Nature* **408**, 944–6 (2000).
- [41] T. C. Schulthess, W. M. Temmerman, Z. Szotek, W. H. Butler, and G. Malcolm Stocks, Electronic structure and exchange coupling of Mn impurities in III-V semiconductors, *Nature Mater.* **4**, 838–844 (2005).
- [42] A. X. Gray, J. Minár, S. Ueda, P. R. Stone, Y. Yamashita, J. Fujii, J. Braun, L. Plucinski, C. M. Schneider, G. Panaccione, H. Ebert, O. D. Dubon, K. Kobayashi, and C. S. Fadley, Bulk electronic structure of the dilute magnetic semiconductor Ga(1-x)Mn(x)As through hard X-ray angle-resolved photoemission., *Nature Mater.* **11**, 957–962 (2012).
- [43] M. Dobrowolska, K. Tivakornsasithorn, X. Liu, J. K. Furdyna, M. Berciu, K. M. Yu, and W. Walukiewicz, Controlling the Curie temperature in (Ga,Mn)As through location of the Fermi level within the impurity band., *Nature Mater.* **11**, 444–449 (2012).

- [44] S. Ohya, K. Takata, and M. Tanaka, Nearly non-magnetic valence band of the ferromagnetic semiconductor GaMnAs, *Nat. Phys.* **7**, 342–347 (2011).
- [45] K. Sato, L. Bergqvist, J. Kudrnovský, P. H. Dederichs, O. Eriksson, I. Turek, B. Sanyal, G. Bouzerar, H. Katayama-Yoshida, V. A. Dinh, T. Fukushima, H. Kizaki, and R. Zeller, First-principles theory of dilute magnetic semiconductors, *Rev. Mod. Phys.* **82**, 1633–1690 (2010).
- [46] D. Kitchen, A. Richardella, J.-M. Tang, M. E. Flatté, and A. Yazdani, Atom-by-atom substitution of Mn in GaAs and visualization of their hole-mediated interactions., *Nature* **442**, 436–9 (2006).
- [47] Y.-J. Zhao, P. Mahadevan, and A. Zunger, Practical rules for orbital-controlled ferromagnetism of 3d impurities in semiconductors, *J. Appl. Phys.* **98**, 113901 (2005).
- [48] P. Mahadevan and A. Zunger, First-principles investigation of the assumptions underlying model-Hamiltonian approaches to ferromagnetism of 3d impurities in III-V semiconductors, *Phys. Rev. B* **69**, 115211 (2004).
- [49] S. Fan, K. Yao, Z. Huang, J. Zhang, G. Gao, and G. Du, Ti-doped AlN potential n-type ferromagnetic semiconductor: Density functional calculations, *Chem. Phys. Lett.* **482**, 62–65 (2009).
- [50] J. M. D. Coey, *Magnetism and magnetic materials*, Cambridge Univ. Press, New York, NY, 2010.
- [51] E. T. Lacheisserie, D. Gignoux, and M. Schlenker, *Magnetism: Fundamentals* (Springer, New York, 2005).
- [52] M. S. Senn, J. P. Wright, and J. P. Attfield, Charge order and three-site distortions in the Verwey structure of magnetite., *Nature* **481**, 173–6 (2012).
- [53] J. M. Zuo, M. Kim, M. O’Keeffe, and J. C. H. Spence, Direct observation of d-orbital holes and Cu-Cu bonding in Cu<sub>2</sub>O, **401**, 49–52 (1999).
- [54] H. Raebiger and T. Fujita, Multiple exchange interactions induced by Jahn-Teller distortions in dilute magnetic semiconductors, *Phys. Rev. B* **84**, 172406 (2011).

- [55] H. Raebiger, S. Lany, and A. Zunger, Impurity Clustering and Ferromagnetic Interactions that are not Carrier Induced in Dilute Magnetic Semiconductors: The Case of Cu<sub>2</sub>O:Co, *Phys. Rev. Lett.* **99**, 167203 (2007).
- [56] ZnTe & CdTe: H. Gürel, O. Akinçi, H. Ünlü, *Superlattices Microstruct.* **51**, 725-732 (2012), MgO, AlN, GaN, GaAs: L. Schimka J. Harl, and G. Kresse, *J. Chem. Phys.* **134**, 024116 (2011).
- [57] III-V semiconductors, ZnTe & CdTe: The Semiconductors-Information Web-Site, <http://www.semiconductors.co.uk>, MgO, CrO<sub>2</sub> & Cr<sub>2</sub>O<sub>3</sub>: D. R. Lide, *CRC Handbook of Chemistry and Physics*, Internet Version 2005, (<http://www.hbcnpnetbase.com>), CRC Press, Boca Raton, FL, 2005.
- [58] S. Lany and A. Zunger, Accurate prediction of defect properties in density functional supercell calculations, *Model. Simul. Mater. Sci. Eng.* **17**, 084002 (2009).
- [59] W. A. Harrison, *Electronic Structure and the Properties of Solids* (W. H. Freeman & Company, San Francisco, 1980).
- [60] M. Rovezzi, F. D'Acapito, A. Navarro-Quezada, B. Faina, T. Li, A. Bonanni, F. Filippone, A. Bonapasta, and T. Dietl, Local structure of (Ga,Fe)N and (Ga,Fe)N:Si investigated by x-ray absorption fine structure spectroscopy, *Phys. Rev. B* **79**, 195209 (2009).
- [61] S. Kuroda, N. Nishizawa, K. Takita, M. Mitome, Y. Bando, K. Osuch, and T. Dietl, Origin and control of high-temperature ferromagnetism in semiconductors., *Nat. Mater.* **6**, 440–6 (2007).
- [62] L.-H. Ye and A. Freeman, Defect compensation, clustering, and magnetism in Cr-doped anatase TiO<sub>2</sub>, *Phys. Rev. B* **73**, 081304 (2006).
- [63] T. Dietl, Self-organized growth controlled by charge states of magnetic impurities., *Nat. Mater.* **5**, 673 (2006).
- [64] T. Fujita and H. Raebiger, Direct d-d interactions among transition metal impurities in III-V semiconductors, *Appl. Phys. Express* **7**, 023004 (2014).
- [65] Control of defect binding and magnetic interaction energies in dilute magnetic semiconductors by charge state manipulation, *J. Appl. Phys.* **115**, 012008 (2014).



- [66] H. Nakayama, T. Fujita, and H. Raebiger, Magnetic Properties and Stability of Quasi-One-Dimensional Cr Chains Embedded in (Zn,Cr)Te, *Appl. Phys. Express* **6**(7), 073006 (June 2013).
- [67] V. I. Anisimov, J. Zaanen, and O. K. Andersen, Band theory and Mott insulators: Hubbard U instead of Stoner I, *Phys. Rev. B* **44**, 943–954 (1991).
- [68] V. I. Anisimov, I. V. Solovyev, and M. A. Korotin, Density-functional theory and NiO photoemission spectra, *Phys. Rev. B* **48**, 16929–16934 (1993).
- [69] S. Lany, J. Osorio-Guillén, and A. Zunger, Origins of the doping asymmetry in oxides: Hole doping in NiO versus electron doping in ZnO, *Phys. Rev. B* **75**, 241203 (2007).
- [70] H. J. Monkhorst and J. D. Pack, Special points for Brillouin-zone integrations, *Phys. Rev. B* **13**, 5188–5192 (1976).
- [71] A. Zunger and U. Lindefelt, Theory of substitutional and interstitial 3d impurities in silicon, *Phys. Rev. B* **26**, 5989–5992 (1982).
- [72] F. Bernardini, V. Fiorentini, and D. Vanderbilt, Spontaneous polarization and piezoelectric constants of III-V nitrides, *Phys. Rev. B* **56**, R10024–R10027 (1997).
- [73] J. Ihm, A. Zunger, and M. L. Cohen, Momentum-space formalism for the total energy of solids, *J. Phys. C Solid State Phys.* **12**, 4409–4422 (1979).
- [74] W. E. Pickett, Pseudopotential methods in condensed matter applications, *Comput. Phys. Reports* **9**, 115–197 (1989).
- [75] M. T. Yin and M. L. Cohen, Theory of lattice-dynamical properties of solids: Application to Si and Ge, *Phys. Rev. B* **26**, 3259–3272 (1982).
- [76] G. Makov and M. Payne, Periodic boundary conditions in ab initio calculations, *Phys. Rev. B* **51**, 4014–4022 (1995).